Supplementary Information (SI) for Physical Chemistry Chemical Physics.

Understanding Electrochemical Reactions using Density Functional Theory: Bridging Theoretical Scheme of Squares and Experimental Cyclic Voltammetry (Supplementary Material)

Amir Mahdian[a], Arsalan Hashemi[a], Kari Laasonen[a]

[a]*Department of chemistry and material science, School of chemical engineering, Aalto University, 02150 Espoo, Finland*

Contents

Email address: `kari.laasonen@aalto.fi` (Kari Laasonen)

1. Current-Potential Relationship

The rates of the reduction and oxidation reactions are expressed as follows:

$$\nu_{\text{red}} = k_{\text{red}}\, c_{\text{ox}}(0,t) = j_c/n_e F \tag{1}$$

$$\nu_{\text{ox}} = k_{\text{ox}}\, c_{\text{red}}(0,t) = j_a/n_e F, \tag{2}$$

where ν_{red} and ν_{ox} represent the rates of reduction and oxidation reactions, j_c and j_a represent the partial cathodic and anodic current densities, respectively. The cathodic current involves electron transfer from an electrode to a species in solution, whereas the anodic current involves electron transfer from a species in solution to an electrode. The terms $c_{\text{ox}}(0,t)$ and $c_{\text{red}}(0,t)$ denote the concentrations of oxidized and reduced forms at the electrode surface, respectively, at time t. Under steady-state conditions, these concentrations are not time-dependent. Additionally, k_{ox} and k_{red} denote the oxidation and reduction rate constants, respectively.

However, if the system is not in equilibrium, the current will flow as described by the following equation:

$$\nu = k_{\text{red}}\, c_{\text{ox}}(x=0) - k_{\text{ox}}\, c_{\text{red}}(x=0) = j/n_e F. \tag{3}$$

For any chemical reaction, the rate constant is related to the Gibbs free energy of activation ($\Delta G^{\dagger}$) using the Arrhenius equation as follows:

$$k = k_{max}\, \exp(-\Delta G^{\dagger}/RT), \tag{4}$$

where k_{max} denotes the upper limit of k.

For a symmetric current-potential diagram, the potential dependence of the rate constants can be expressed as follows:

$$k_{\text{red}} = k_{\text{max}}\, \exp\Big[-n_e F(E_{\text{appl}} - E^0_{\text{ox/red}})/2RT\Big] \tag{5}$$

$$k_{\text{ox}} = k_{\text{max}}\, \exp\Big[n_e F(E_{\text{appl}} - E^0_{\text{ox/red}})/2RT\Big]. \tag{6}$$

Here, E_{appl} represents the electrode's applied potential.

At equilibrium, the electrochemical current j is equal to zero, $j_a = |j_c| = j_0$ (indicating dynamic equilibrium) and no difference exists between the surface and bulk concentrations. By integrating Eqs. (5 and 6) into Eq. (3), one derives

$$n_e F\; (E_{\text{appl}} - E^0_{\text{ox/red}})/RT = c_{\text{ox}}/c_{\text{red}} \tag{7}$$

Finally, the expression for j_0 as a function of E_{appl} is given by

$$j_0 = -n_e F k_{max}\, c_{\text{ox}} \exp[-\alpha n_e F (E_{\text{appl}} - E^0_{\text{ox/red}})/RT], \tag{8}$$

where α is the transfer coefficient. For a symmetric barrier, $\alpha = 0.5$, but generally ranges from 0 to 1.

2. OTDFL Proton-Electron Transfer Reactions at Different pH Values

In this Supplementary Material, all values except those in Figure S3 are computed with 6-31G(d)-Def2TZVP method.

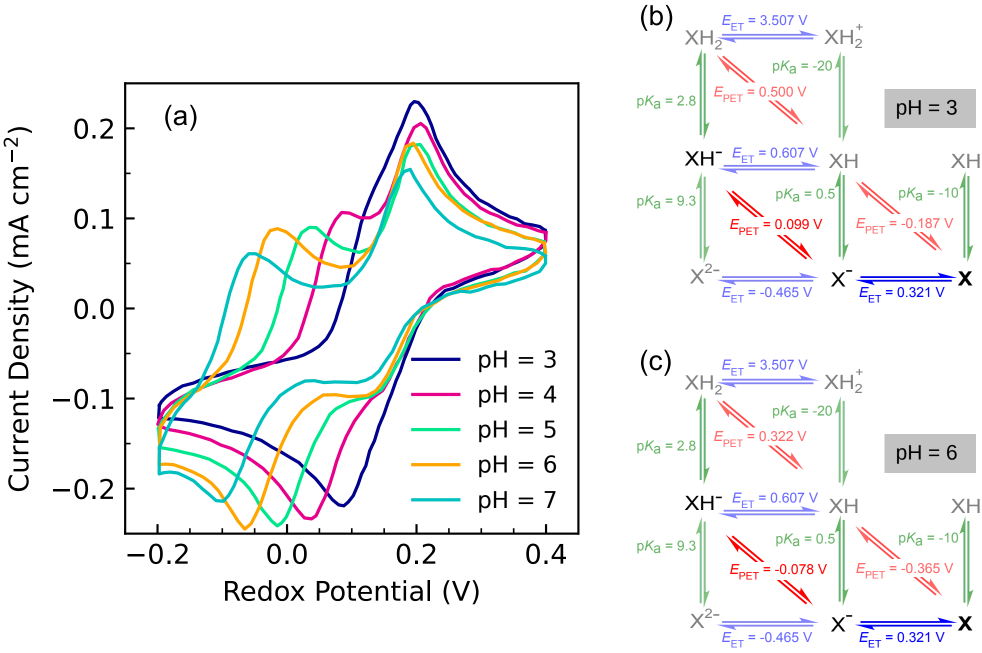

Figure 1: (a) Experimental cyclic voltammetry of the OTDFL at t different pH values from 3 to 7 extracted from Ref. [1]. The scheme of squares are illustrated to assess the pH-dependent reaction pathways at (b) pH 3 and (c) pH 6. In these diagrams, vertical arrows represent proton transfer (PT) reactions, horizontal arrows indicate electron transfer (ET) reactions, and diagonal arrows denote proton-electron transfer (PET) reactions. PT is quantified by $\mathrm{p}K_\mathrm{a}$, while ET and PET are assessed by redox potential in V_SHE. The formal redox potential is shown by a vertical dashed line.

Compound OTDFL undergoes a one-electron transfer (ET) followed by a proton-electron transfer (PET) at pH of 6, shown in Figure 1 (a). In spite of it being challenging to detect such a dual process at low pH values (e.g., pH = 3), the transition from a shoulder to a well-defined peak at a lower potential—as the pH is raised—provides strong evidence of this phenomenon. The initial electron transfer (ET) occurs at 0.16 V_SHE in the experiment[1]. However, our calculated data indicates an overestimation, showing 0.321 V_SHE. This value is constant and independent of pH. The interpretation of the scheme of squares will be in a better agreement with the experiments if one includes the scaling relations, cf. Section 4. The PET reaction is pH-dependent, with variations in redox potential modeled by the Nernst equation. Notably, at a pH of 3, Figure 1 (b), the more acidic conditions facilitate proton sourcing, resulting in a higher redox potential compared to pH of 6 1 (c). In its reduced form, compound **XH**$^{-}$ is chemically inert. The pK_{a} values of 9.3 and 2.8 prevents protonation and deprotonation processes at pH ranges from 3 to 7. An oxidative potential is applied in reverse to form **X** species.

3. Dihedral Angle Scanning in 9-Fluorenone-1-carboxylic acid Radicals

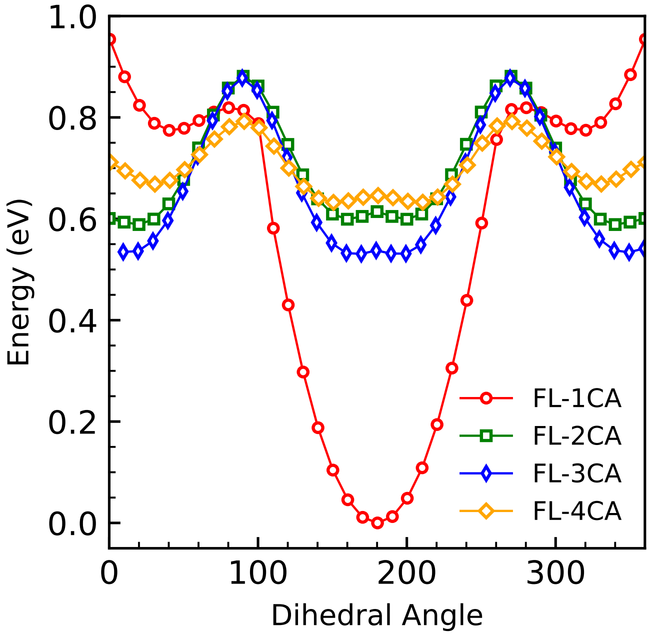

Figure 2: Energy versus dihedral angles for different FL-nCA derivatives, where $n = 1, 2, 3, 4$, as shown in Figure 2(a).

The hydrogen bond formation between oxygen in ketone (C=O) of FL-nCA derivatives and hydrogen in its carboxylic acid (COOH) was investigated by scanning the dihedral angles of the (COOH) and the benzene ring. The dihedral angle is defined by the following atoms: the oxygen atom (O) in the hydroxy group (OH) of the carboxylic acid (COOH), the carbon atom (C) of the COOH group directly bonded to this oxygen, the carbon atom (C) at the attachment site of the FL-nCA, and its neighboring carbon atom in the chain. All the compounds are in their radical forms (XH). Figure 2 illustrates total energy variations versus dihedral angles.

When the dihedral angle is 0 degrees, the OH of the carboxylic acid (COOH) group is perfectly aligned in the molecular plane, H directly pointing towards the oxygen atom of the ketone (C=O), which is an optimal orientation for hydrogen bond formation. Our results show that the COOH group positioned next to the ketone (FL-1CA) while its H atom shared with ketone group offered the most favorable arrangement. This stability arises from hydrogen bonding between the carboxylic acid hydrogen and the ketone. The remaining configurations (FL-2CA, FL-3CA, FL-4CA) exhibit energy profiles that are nearly identical.

4. ET and PET Reactions Redox Potential Linear Scaling

Datasets comprising 60 and 40 molecules were compiled from different peer-reviewed studies to analyze electron transfer (ET) and proton-electron transfer (PET) redox potentials, respectively. These selections were based on specific criteria related to their relevance and impact in the field of redox chemistry, ensuring a comprehensive analysis of redox behaviors. For a comprehensive overview of the datasets, including detailed descriptions of the reaction process and references, refer to Sections 5 and 6. In Figure S3 two different computational methods were employed to calculate these molecules: the more accurate but expensive 6-31G(d)-Def2TZVP and the less time-consuming and less accurate semi-empirical method PM7-Def2TZVP. The obtained results show similar almost accuracy for ET reactions. Thought, the deviation of PET redox potentials from experiments is stronger that could be due to the slope of Nernst equations that might deviate from 0.059 due to different external conditions. To compile the PET and/or ET processes, we draw the scheme of squares of all the molecules in the following from S4 onwards.

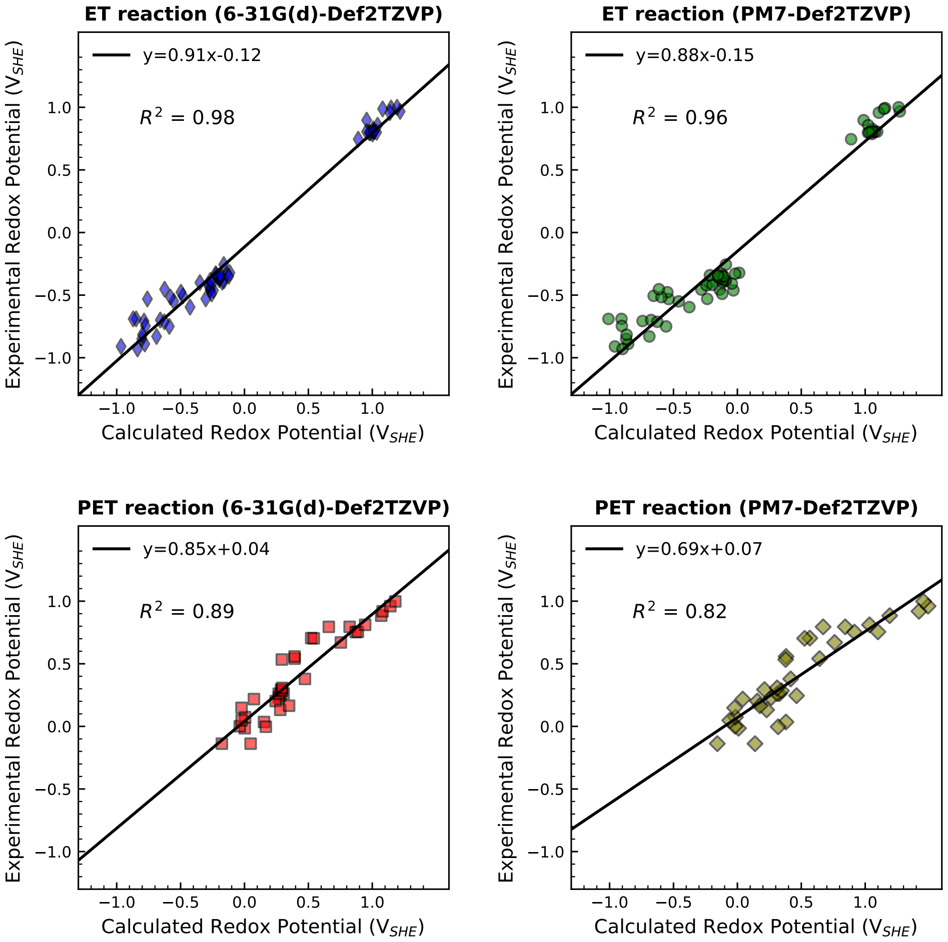
ET reaction (6-31G(d)-Def2TZVP)

ET reaction (PM7-Def2TZVP)

PET reaction (6-31G(d)-Def2TZVP)

PET reaction (PM7-Def2TZVP)

Figure 3: Scaling of calculated redox potentials of the ET and PET reactions against experimental data. Calculations were performed using two computational setups: 6-31G(d)-Def2TZVP and PM7-Def2TZVP. Each subplot includes the linear regression model formula along with the coefficient of determination (R^2).

5. Dataset of Molecules for Electron Transfer Reactions

Below is a list of molecules, with abbreviated names and experimental references, considered for scaling the redox potential of electron transfer (ET) reactions. The associated experimental and computational redox potentials (versus SHE) are included. The measured redox potential is the mid-peak potential taken from CV diagram. Detailed molecular structures and computational inputs are available for download from the ***Zenodo database****.*

1. DMAE-Pr2-Vi, $E^0_{expt.} = -0.332$ V Ref. [2], $E^0_{dft} = -0.14$ V

2. FL-R2, $E^0_{expt.} = -0.690$ V Ref. [3], $E^0_{dft} = -0.848$ V

3. FL-R4, $E^0_{expt.} = -0.690$ V Ref. [3], $E^0_{dft} = -0.871$ V

4. 4OH-TEMPO, $E^0_{expt.} = 0.798$ V Ref. [4], $E^0_{dft} = 0.976$ V

5. Methylviologen, $E^0_{expt.} = -0.456$ V Ref. [5], $E^0_{dft} = -0.267$ V

6. Ethylviologen, $E^0_{expt.} = -0.456$ V Ref. [5], $E^0_{dft} = -0.267$ V

7. Benzoylviologen, $E^0_{expt.} = -0.256$ V Ref. [5], $E^0_{dft} = -0.162$ V

8. SPr2-viologen, $E^0_{expt.} = -0.400$ V Ref. [6], $E^0_{dft} = -0.349$ V

9. R-viologen, $E^0_{expt.} = -0.550$ V Ref. [6], $E^0_{dft} = -0.553$ V

10. NMe-TEMPO, $E^0_{expt.} = 0.994$ V Ref. [7], $E^0_{dft} = 1.147$ V

11. NPr2TTz (1st ET), $E^0_{expt.} = -0.386$ V Ref. [8], $E^0_{dft} = -0.161$ V

12. NPr2TTz (2nd ET), $E^0_{expt.} = -0.506$ V Ref. [8], $E^0_{dft} = -0.482$ V

13. 1-1-Bispropyl-4-4-bipyridinium, $E^0_{expt.} = -0.423$ V Ref. [9], $E^0_{dft} = -0.282$ V

14. 1-1-Bisbutyl-4-4-bipyridinium, $E^0_{expt.} = -0.418$ V Ref. [9], $E^0_{dft} = -0.274$ V

15. BPP-Vi (1st ET), $E^0_{expt.} = -0.243$ V Ref. [10], $E^0_{dft} = -0.462$ V

16. BPP-Vi (2nd ET), $E^0_{expt.} = -0.890$ V Ref. [10], $E^0_{dft} = -0.780$ V

17. BHOE, $E^0_{expt.} = -0.408$ V Ref. [11], $E^0_{dft} = -0.254$ V

18. Pyr-PV, $E^0_{expt.} = -0.531$ V Ref. [12], $E^0_{dft} = -0.760$ V

19. Pyr-TEMPO, $E^0_{expt.} = 0.805$ V Ref. [12], $E^0_{dft} = 1.015$ V

20. PV, $E^0_{expt.} = -0.383$ V Ref. [13], $E^0_{dft} = -0.268$ V

21. Me-NPr-Vi (1st ET), $E^0_{expt.} = -0.396$ V Ref. [14], $E^0_{dft} = -0.174$ V

22. Me-NPr-Vi (2nd ET), $E^0_{expt.} = -0.707$ V Ref. [14], $E^0_{dft} = -0.786$ V

23. SPr-NPr-Vi (1st ET), $E^0_{expt.} = -0.376$ V Ref. [14], $E^0_{dft} = -0.197$ V

24. SPr-NPr-Vi (2nd ET), $E^0_{expt.} = -0.746$ V Ref. [14], $E^0_{dft} = -0.775$ V

25. exBP, $E^0_{expt.} = -0.750$ V Ref. [15], $E^0_{dft} = -0.588$ V

26. exBP-Me, $E^0_{expt.} = -0.830$ V Ref. [15], $E^0_{dft} = -0.688$ V

27. exBP-DMe, $E^0_{expt.} = -0.910$ V Ref. [15], $E^0_{dft} = -0.966$ V

28. Dex-Vi (1st ET), $E^0_{expt.} = -0.322$ V Ref. [16], $E^0_{dft} = -0.114$ V

29. Dex-Vi (2nd ET), $E^0_{expt.} = -0.699$ V Ref. [16], $E^0_{dft} = -0.659$ V

30. Ets (1st ET), $E^0_{expt.} = -0.341$ V Ref. [17], $E^0_{dft} = -0.222$ V

31. BPP-mVi (1st ET), $E^0_{expt.} = -0.53$ V Ref. [10], $E^0_{dft} = -0.303$ V

32. BPP-mVi (2nd ET), $E^0_{expt.} = -0.930$ V Ref. [10], $E^0_{dft} = -0.837$ V

33. BTMAP-mVi (1st ET), $E^0_{expt.} = -0.490$ V Ref. [10], $E^0_{dft} = -0.257$ V

34. BTMAP-mVi (2nd ET), $E^0_{expt.} = -0.850$ V Ref. [10], $E^0_{dft} = -0.804$ V

35. BTMAP-Vi (1st ET), $E^0_{expt.} = -0.349$ V Ref. [16], $E^0_{dft} = -0.123$ V

36. BTMAP-Vi (2nd ET), $E^0_{expt.} = -0.713$ V Ref. [16], $E^0_{dft} = -0.627$ V

37. DiOH (1st ET), $E^0_{expt.} = -0.366$ V Ref. [17], $E^0_{dft} = -0.194$ V

38. EtS-DiOH (1st ET), $E^0_{expt.} = -0.354$ V Ref. [17], $E^0_{dft} = -0.203$ V

39. SHOP-DiOH, $E^0_{expt.} = -0.352$ V Ref. [17], $E^0_{dft} = -0.193$ V

40. SHOP-Dex (1st ET), $E^0_{expt.} = -0.329$ V Ref. [17], $E^0_{dft} = -0.225$ V

41. Dex-DiOH, $E^0_{expt.} = -0.342$ V Ref. [17], $E^0_{dft} = -0.189$ V

42. TEMPO, $E^0_{expt.} = 0.745$ V Ref. [18], $E^0_{dft} = 0.890$ V

43. NPr2FV (1st ET), $E^0_{expt.} = -0.596$ V Ref. [19], $E^0_{dft} = -0.426$ V

44. NPr2FV (2nd ET), $E^0_{expt.} = -0.816$ V Ref. [19], $E^0_{dft} = -0.798$ V

45. TEMPO-Viologen, $E^0_{expt.} = 0.973$ V Ref. [20], $E^0_{dft} = 1.165$ V

46. 2_2_PEAQ, $E^0_{expt.} = -0.477$ V Ref. [21], $E^0_{dft} = -0.497$ V

47. 3_NH2_2_2PEAG, $E^0_{expt.} = -0.516$ V Ref. [22], $E^0_{dft} = -0.579$ V

48. 2_6_D2PEA, $E^0_{expt.} = -0.453$ V Ref. [23], $E^0_{dft} = -0.625$ V

49. TMAP_TEMPO, $E^0_{expt.} = 0.810$ V Ref. [4], $E^0_{dft} = 1.015$ V

50. N2TEMPO, $E^0_{expt.} = 1.000$ V Ref. [7], $E^0_{dft} = 1.194$ V

51. 4_Amino_TEMPO, $E^0_{expt.} = 0.897$ V Ref. [24], $E^0_{dft} = 0.956$ V

52. 4_COOH_TEMPO, $E^0_{expt.} = 0.787$ V Ref. [24], $E^0_{dft} = 1.002$ V

53. 4_NHCOCH3_TEMPO, $E^0_{expt.} = 0.827$ V Ref. [24], $E^0_{dft} = 1.007$ V

54. PSS_TEMPO, $E^0_{expt.} = 0.805$ V Ref. [25], $E^0_{dft} = 0.955$ V

55. CPL, $E^0_{expt.} = 0.957$ V Ref. [26], $E^0_{dft} = 1.138$ V

56. CPD, $E^0_{expt.} = 0.857$ V Ref. [26], $E^0_{dft} = 1.042$ V

57. CT, $E^0_{expt.} = 0.797$ V Ref. [26], $E^0_{dft} = 0.983$ V

58. TEMPO_4_sulfate, $E^0_{expt.} = 0.807$ V Ref. [27], $E^0_{dft} = 1.008$ V

59. g+_TEMPO, $E^0_{expt.} = 0.8$ V Ref. [27], $E^0_{dft} = 1.034$ V

60. TEMPO-imidazolium, $E^0_{expt.} = 0.987$ V Ref. [27], $E^0_{dft} = 1.081$ V

6. Dataset of Molecules for Proton-Electron Transfer Reactions

Below is a list of molecules, with names and experimental references, considered for scaling the redox potential of proton-electron transfer (PET) reactions. The related experimental cyclic voltammogram (CV) and computational scheme of squares are included. The measured redox potential is the mid-peak potential taken from CV diagram. Detailed molecular structures and computational inputs are available to for download from the ***Zenodo database****. For compounds where XH_2 undergoes further protonation reaction, the scheme of squares will be demonstrated.*

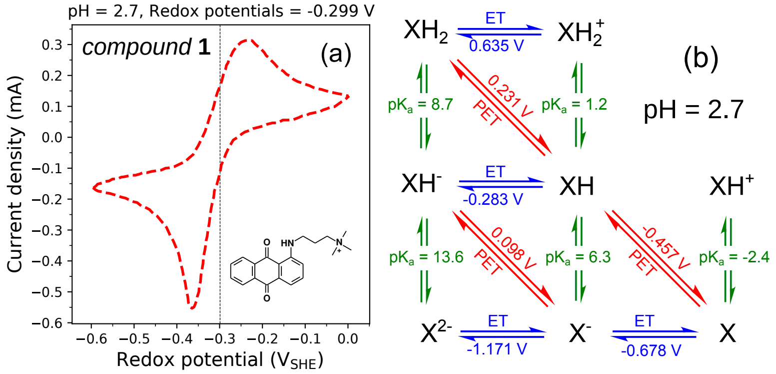

Figure 4: (a) Experimental CV of *compound* **1** accompanied by molecular structure in its oxidized form taken form Ref. [28]. The measured redox potential is indicated by a vertical dashed line. (b) The scheme of squares at pH of 2.7, where the vertical, horizontal, and diagonal arrows indicate PT, ET, and PET reactions, respectively. PT is quantified by pK_a, while ET and PET are assessed by redox potentials ($\mathrm{V_{SHE}}$).

Compound **1**, shown in Figure 4, is named ”3-((9,10-dioxo-9,10-dihydroanthracen-1-yl)amino)-N,N,N-trimethylpropan-1-aminium chloride” (1-DPAQCl). During a reduction reaction, it accepts 2 protons and 2 electrons through proton-electron transfer (PET) reactions. These reactions are reversible. The redox potential for the 2PET process is approximately -0.113 $\mathrm{V_{SHE}}$, while the experimental value is measured at -0.299 $\mathrm{V_{SHE}}$.

The redox potential of 2PET reaction is computed as follows:

$$E = -\frac{\Delta G}{n_e e} = \frac{E_{\mathrm{X-XH}} + E_{\mathrm{XH-XH_2}}}{2}, \tag{9}$$

where E represents the average redox potential, ΔG is the Gibbs free energy change for the reaction, n_e is the number of electrons transferred in the reaction, and e is the elementary charge. The terms $E_{\mathrm{X-XH}}$ and $E_{\mathrm{XH-XH_2}}$ represent the redox potentials for the first and second PET reactions, specifically from X to XH and from XH to $\mathrm{XH_2}$, respectively. The H of amine group shows pK_a of 12.7.

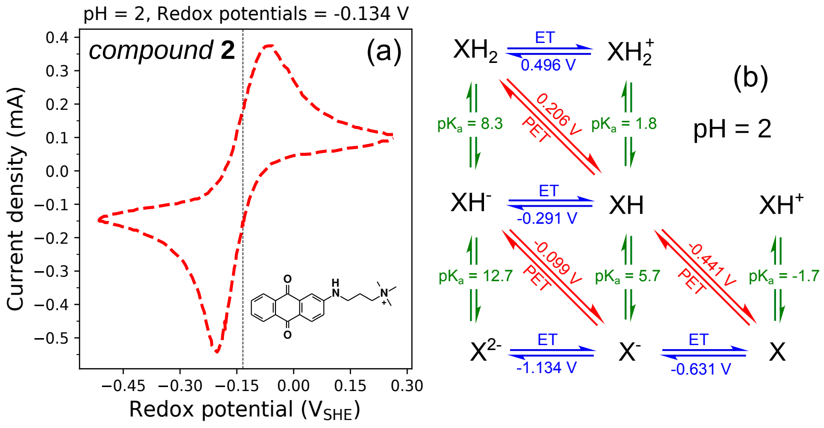

Figure 5: (a) Experimental CV of *compound* **2** accompanied by molecular structure in its oxidized form taken form Ref. [28]. The measured redox potential is indicated by a vertical dashed line. (b) The scheme of squares at pH of 2, where the vertical, horizontal, and diagonal arrows indicate PT, ET, and PET reactions, respectively. PT is quantified by pK_a, while ET and PET are assessed by redox potentials ($\mathrm{V_{SHE}}$).

Compound **2**, shown in Figure 5, is named ”3-((9,10-dioxo-9,10-dihydroanthracen-2-yl)amino)-N,N,N-trimethylpropan-1-aminium chloride” (2-DPAQCl). In the course of reduction reaction, it undergoes 2PET reactions: X to XH and from XH to XH_2. This reaction is reversible. The redox potential is approximately -0.118 $\mathrm{V_{SHE}}$, while the experimental value is measured at -0.134 $\mathrm{V_{SHE}}$. The H of amine group shows pK_a of 13.9 which means it does not deprotonate at pH of 2.

Compound **3**, shown in Figure 6, is named ”Dopamine” (DP). During the redox reaction, it participates in a 2PET reversible reaction. The calculated redox potential is about 0.585 $\mathrm{V_{SHE}}$, whereas the experimental value is measured at 0.557 $\mathrm{V_{SHE}}$.

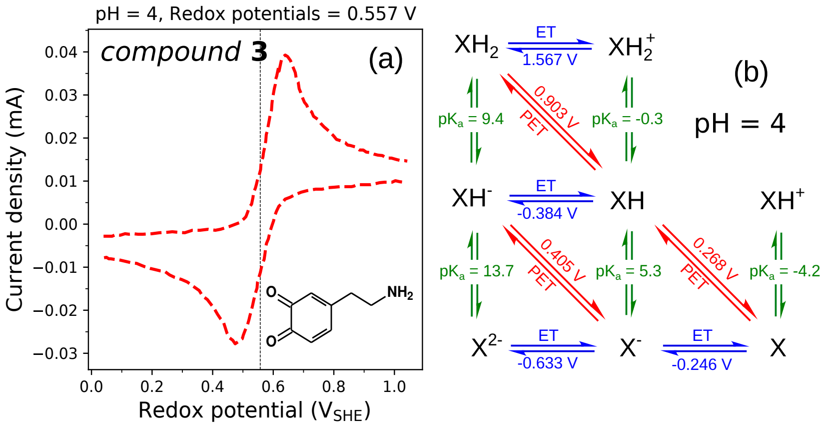

Figure 6: (a) Experimental CV of *compound* **3** accompanied by molecular structure in its oxidized form taken form Ref. [29]. The measured redox potential is indicated by a vertical dashed line. (b) The scheme of squares at pH of 4, where the vertical, horizontal, and diagonal arrows indicate PT, ET, and PET reactions, respectively. PT is quantified by pK_a, while ET and PET are assessed by redox potentials (V_{SHE}).

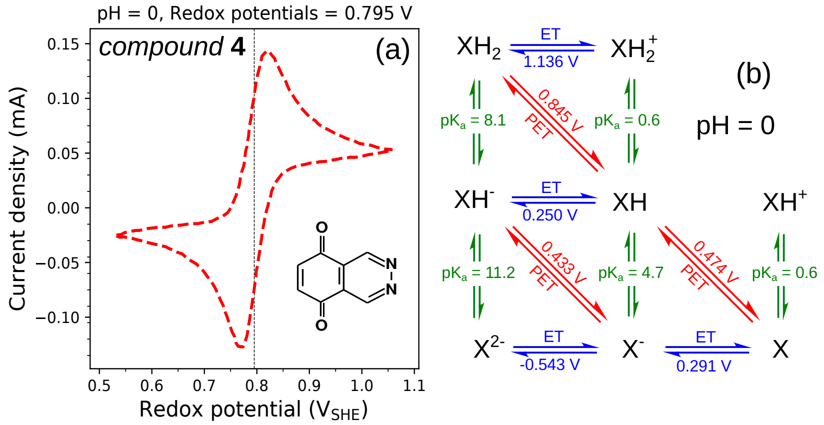

Figure 7: (a) Experimental CV of *compound* **4** accompanied by molecular structure in its oxidized form taken form Ref. [30]. The measured redox potential is indicated by a vertical dashed line. (b) The scheme of squares at pH of 0, where the vertical, horizontal, and diagonal arrows indicate PT, ET, and PET reactions, respectively. PT is quantified by pK_a, while ET and PET are assessed by redox potentials (V_{SHE}).

Compound **4**, illustrated in Figure 7, is named ”5,8-dihydroxy-2,3-phthalazine” (DHP). During the redox reaction, it accepts 2 protons and 2 electrons through the proton-electron transfer (PET) reactions. This reaction is reversible. The calculated redox potential is about 0.660 V_{SHE}, while the experimental value is measured at 0.795 V_{SHE}.

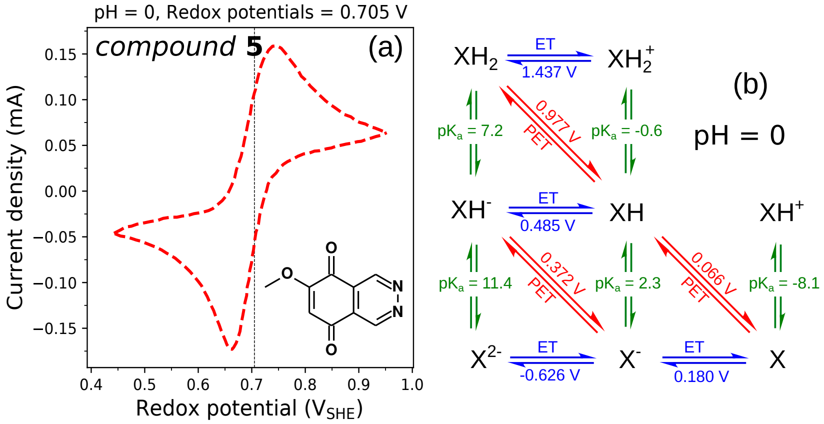

Figure 8: (a) Experimental CV of *compound* **5** accompanied by molecular structure in its oxidized form taken form Ref. [30]. The measured redox potential is indicated by a vertical dashed line. (b) The scheme of squares at pH of 0, where the vertical, horizontal, and diagonal arrows indicate PT, ET, and PET reactions, respectively. PT is quantified by $\mathrm{p}K_{\mathrm{a}}$, while ET and PET are assessed by redox potentials (V_{SHE}).

Compound **5**, shown in Figure 8, is named ”5,8-dihydroxy-6-methoxy-2,3-phthalazine” (DHPMeO). In the course of reduction reaction, the species undergoes 2PET reaction. This reaction is reversible. The redox potential is 0.522 V_{SHE}, whereas the experimental value is measured at 0.705 V_{SHE}.

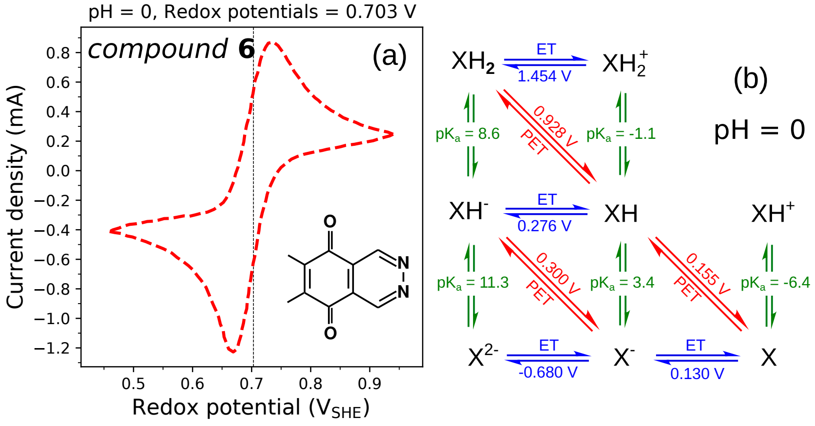

Figure 9: (a) Experimental CV of *compound* **6** accompanied by molecular structure in its oxidized form taken form Ref. [30]. The measured redox potential is indicated by a vertical dashed line. (b) The scheme of squares at pH of 0, where the vertical, horizontal, and diagonal arrows indicate PT, ET, and PET reactions, respectively. PT is quantified by pK_a, while ET and PET are assessed by redox potentials (V_SHE).

Compound **6**, shown in Figure 9, is named ”5,8-dihydroxy-6,7-dimethyl-2,3-phthalazine” (DHP(Me)$_2$). In the redox process, it undergoes a reversible 2PET reaction. The redox potential is approximately 0.542 V_SHE, while the experimental value is measured at 0.703 V_SHE.

Compound **7**, shown in Figure 10, is named ”1,4-dihydroxybenzene” (p-HBQ). A reduction reaction proceeds via a two-step proton-electron transfer (2PET) pathway and is reversible. The calculated redox potential for this reaction is 0.754 V_SHE. The experimental value has been measured at 0.670 V_SHE.

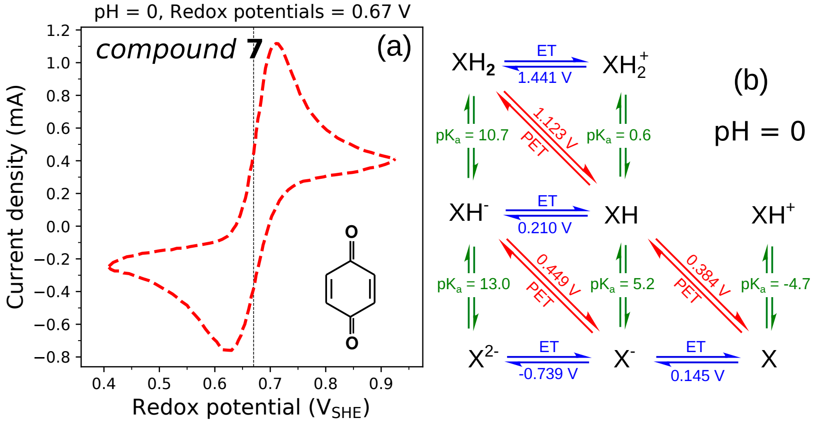

Figure 10: (a) Experimental CV of *compound* **7** accompanied by molecular structure in its oxidized form taken form Ref. [30]. The measured redox potential is indicated by a vertical dashed line. (b) The scheme of squares at pH of 0, where the vertical, horizontal, and diagonal arrows indicate PT, ET, and PET reactions, respectively. PT is quantified by $\mathrm{p}K_\mathrm{a}$, while ET and PET are assessed by redox potentials (V_SHE).

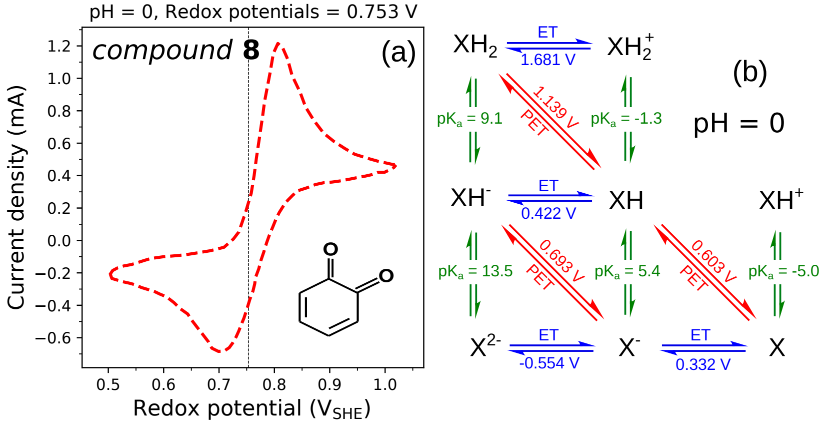

Figure 11: (a) Experimental CV of *compound* **8** accompanied by molecular structure in its oxidized form taken form Ref. [30]. The measured redox potential is indicated by a vertical dashed line. (b) The scheme of squares at pH of 0, where the vertical, horizontal, and diagonal arrows indicate PT, ET, and PET reactions, respectively. PT is quantified by $\mathrm{p}K_\mathrm{a}$, while ET and PET are assessed by redox potentials (V_SHE).

Compound **8**, shown in Figure 11, is named ”1,2-dihydroxybenzene” (o-HBQ). During a reduction reaction, it accepts 2 protons and 2 electrons through proton-electron transfer (PET) reactions. This reaction is reversible. The redox potential for the 2PET process is approximately 0.871 V_{SHE}, while the experimental value is measured at 0.753 V_{SHE}.

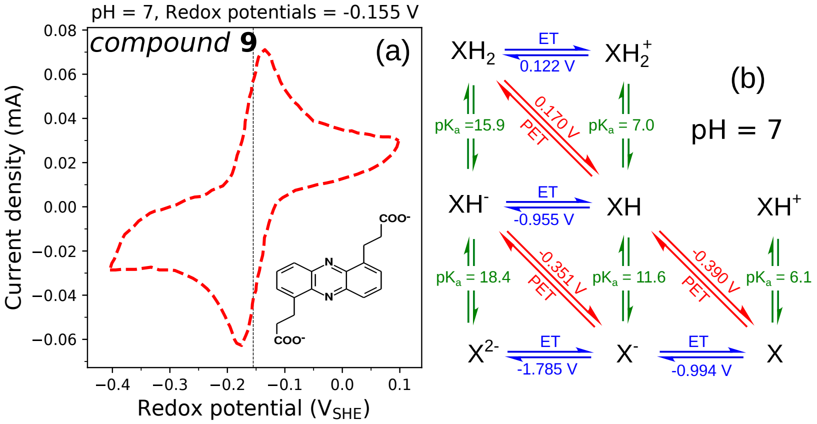

Figure 12: (a) Experimental CV of *compound* **9** accompanied by molecular structure in its oxidized form taken form Ref. [31]. The measured redox potential is indicated by a vertical dashed line. (b) The scheme of squares at pH of 7, where the vertical, horizontal, and diagonal arrows indicate PT, ET, and PET reactions, respectively. PT is quantified by $\mathrm{p}K_{\mathrm{a}}$, while ET and PET are assessed by redox potentials (V_{SHE}).

Compound **9**, shown in Figure 12, is named ”3,3’-(phenazine-1,6-diyl)dipropionic acid” (1,6-PFP). During the reduction reaction, the molecule accepts 2 protons and 2 electrons through the 2PET reaction. This reaction is reversible. The redox potential for the 2PET process is approximately -0.110 V_{SHE}, while the experimental value was measured to be -0.155 V_{SHE}.

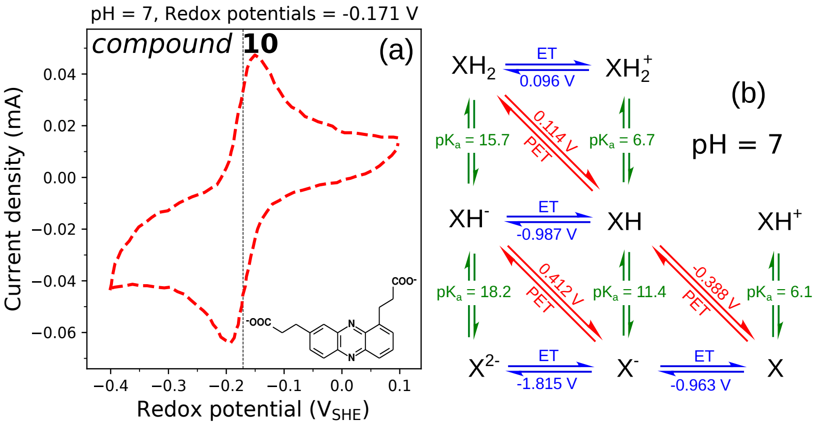

Figure 13: (a) Experimental CV of *compound* **10** accompanied by molecular structure in its oxidized form taken form Ref. [31]. The measured redox potential is indicated by a vertical dashed line. (b) The scheme of squares at pH of 7, where the vertical, horizontal, and diagonal arrows indicate PT, ET, and PET reactions, respectively. PT is quantified by pK_a, while ET and PET are assessed by redox potentials ($\mathrm{V_{SHE}}$).

Compound **10**, shown in Figure 13, is named ”3,3’-(phenazine-1,8-diyl)dipropionic acid” (1,8-PFP). The PET reactions occur during a reduction reaction. The reaction is reversible. Compared to the computed redox potential for the 2PET process, which is almost -0.137 $\mathrm{V_{SHE}}$, the observed experimental value is -0.171 $\mathrm{V_{SHE}}$.

Compound **11**, shown in Figure 14, is named ”3,3’-(phenazine-2,7-diyl)dipropionic acid” (2,7-PFP). In the reduction reaction, the species undergoes the PET reactions to accept two protons and two electrons. This reaction is reversible. The calculated redox potential for such a mechanism is roughly -0.148 $\mathrm{V_{SHE}}$, whereas the experimental value is measured at -0.187 $\mathrm{V_{SHE}}$.

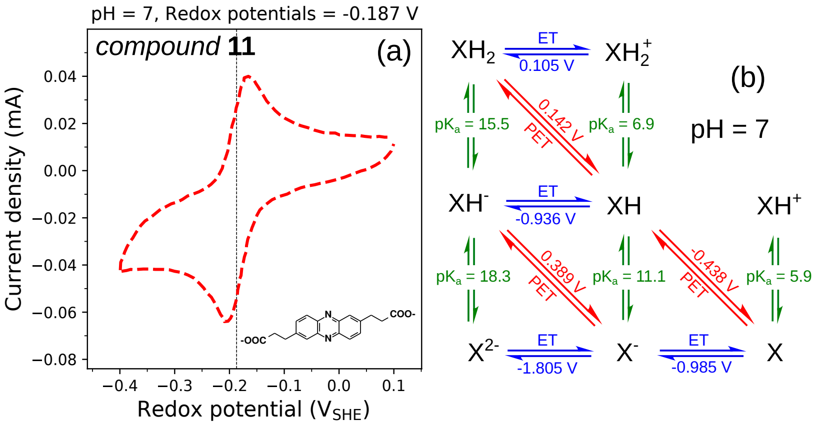

Figure 14: (a) Experimental CV of *compound* **11** accompanied by molecular structure in its oxidized form taken form Ref. [31]. The measured redox potential is indicated by a vertical dashed line. (b) The scheme of squares at pH of 7, where the vertical, horizontal, and diagonal arrows indicate PT, ET, and PET reactions, respectively. PT is quantified by pK_a, while ET and PET are assessed by redox potentials ($\mathrm{V_{SHE}}$).

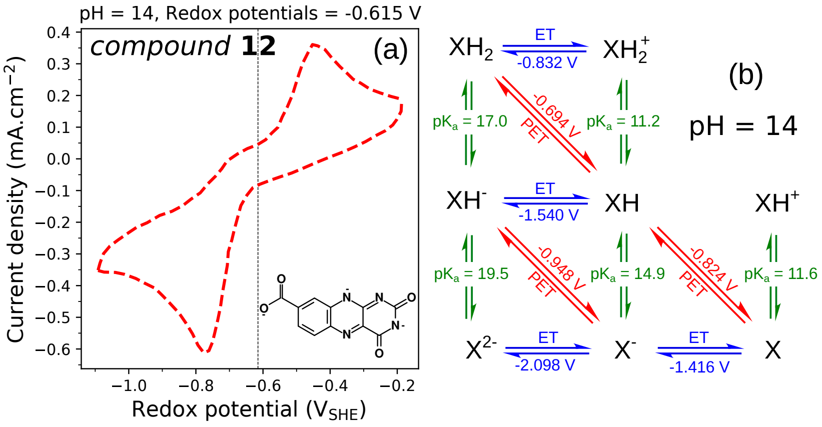

Figure 15: (a) Experimental CV of *compound* **12** accompanied by molecular structure in its oxidized form taken form Ref. [32]. The measured redox potential is indicated by a vertical dashed line. (b) The scheme of squares at pH of 14, where the vertical, horizontal, and diagonal arrows indicate PT, ET, and PET reactions, respectively. PT is quantified by pK_a, while ET and PET are assessed by redox potentials ($\mathrm{V_{SHE}}$).

Compound **12**, shown in Figure 15, is named ”7/8-carboxylic acid” (ACA). The redox reaction occurs through the 2PET reaction which is reversible. The calculated redox potential is -0.759 $\mathrm{V_{SHE}}$, whereas the experimental potential is

-0.615 V_{SHE}. Note that the oxidation reaction of XH_2 is also possible via the ET-PT-PET pathway.

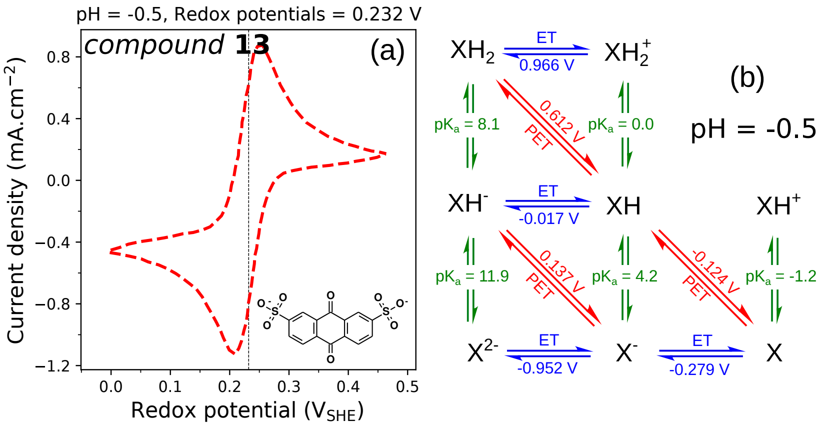

Figure 16: (a) Experimental CV of *compound* **13** accompanied by molecular structure in its oxidized form taken form Ref. [33]. The measured redox potential is indicated by a vertical dashed line. (b) The scheme of squares at pH of -0.5, where the vertical, horizontal, and diagonal arrows indicate PT, ET, and PET reactions, respectively. PT is quantified by pK_a, while ET and PET are assessed by redox potentials (V_{SHE}).

Compound **13**, depicted in Figure 16, is named as ”9,10-anthraquinone-2,7-disulfonic acid” (AQDS). During the reduction reaction, the molecule engages in a reversible 2PET process. The calculated redox potential for this reaction is about 0.244 V_{SHE}. The experimental value is slightly lower, measured at 0.232 V_{SHE}.

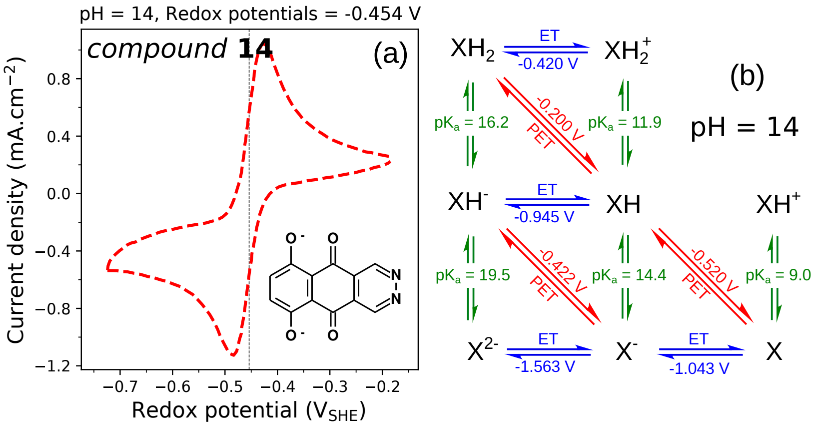

Figure 17: (a) Experimental CV of *compound* **14** accompanied by molecular structure in its oxidized form taken form Ref. [33]. The measured redox potential is indicated by a vertical dashed line. (b) The scheme of squares at pH of 14, where the vertical, horizontal, and diagonal arrows indicate PT, ET, and PET reactions, respectively. PT is quantified by pK_a, while ET and PET are assessed by redox potentials (V_{SHE}).

Compound **14**, depicted in Figure 17, is named as ”2,3-diaza-5,8-dihydroxy-anthracene-9,10-dione” (DADdi(OH)). In the reduction reaction, the molecule accepts 2 protons and 2 electrons via a reversible PET process. The calculated standard redox potential for this 2PET reaction is -0.360 V_{SHE}, compared to the experimental value of -0.454 V_{SHE}. Note that the oxidation reaction of XH_2 is also possible via the ET-PT-PET pathway.

Compound **15**, depicted in Figure 18, is named as ”2,2′-((9,10-dioxo-9,10-dihydroanthracene-1,4-diyl)bis(azanediyl)) bis(N,N,N-trimethylethan-1-aminium)dichloride” ($BDEAQCl_2$). During the reduction reaction, the molecule reversibly accepts two protons and two electrons through a PET process. The calculated redox potential for this 2PET reaction is approximately -0.594 V_{SHE}, compared to the experimental value of -0.555 V_{SHE}. From the scheme of squares, one can see that the ET-PET-PT pathway is also available for redox reactions. While kinetics govern the dominated mechanism, the average redox potential of 2PET is more favorable, making it the more likely pathway.

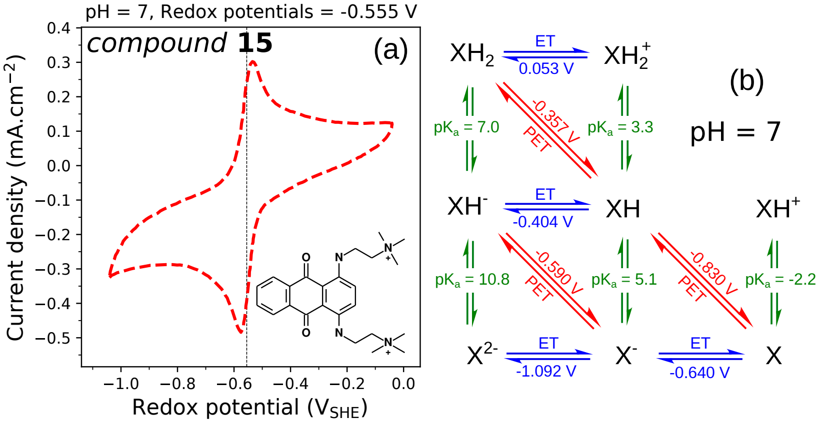

Figure 18: (a) Experimental CV of *compound* **15** accompanied by molecular structure in its oxidized form taken form Ref. [34]. The measured redox potential is indicated by a vertical dashed line. (b) The scheme of squares at pH of 7, where the vertical, horizontal, and diagonal arrows indicate PT, ET, and PET reactions, respectively. PT is quantified by pK_a, while ET and PET are assessed by redox potentials ($\mathrm{V_{SHE}}$).

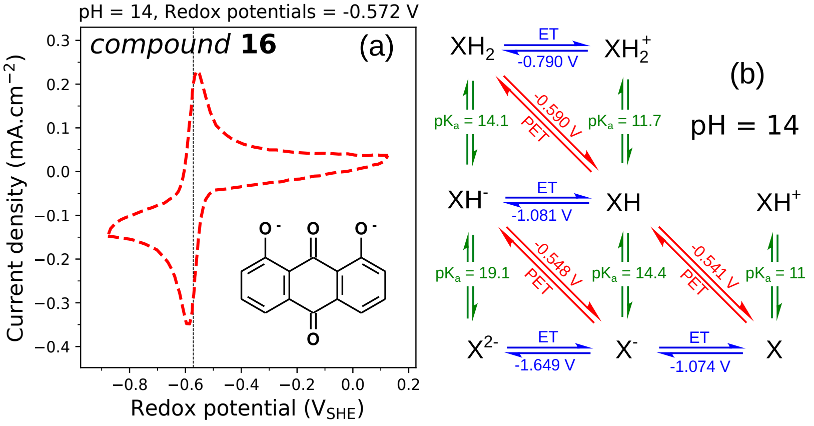

Figure 19: (a) Experimental CV of *compound* **16** accompanied by molecular structure in its oxidized form taken form Ref. [35]. The measured redox potential is indicated by a vertical dashed line. (b) The scheme of squares at pH of 14, where the vertical, horizontal, and diagonal arrows indicate PT, ET, and PET reactions, respectively. PT is quantified by pK_a, while ET and PET are assessed by redox potentials ($\mathrm{V_{SHE}}$).

Compound **16**, depicted in Figure 19, is named as ”1,8-dihydroxyanthraquinone” (1,8-DHAQ). In the reduction reaction, the molecule undergoes 2PET process. The calculated redox potential for the 2PET reaction is

-0.565 V_{SHE}, slightly higher than the experimental value of -0.572 V_{SHE}.

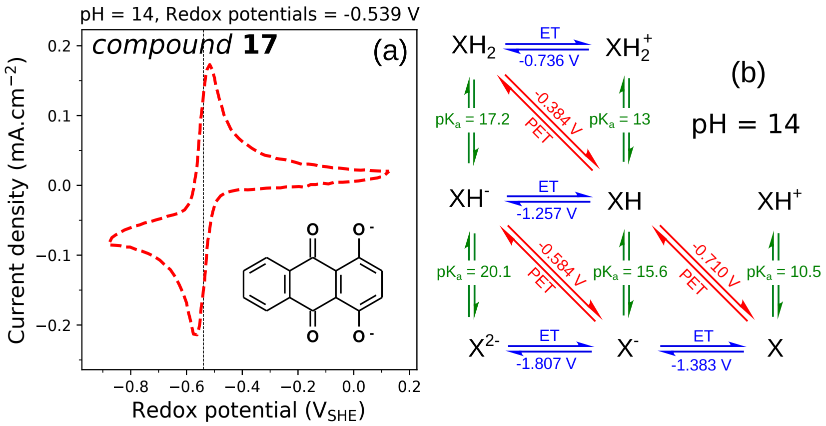

Figure 20: (a) Experimental CV of *compound* **17** accompanied by molecular structure in its oxidized form taken form Ref. [35]. The measured redox potential is indicated by a vertical dashed line. (b) The scheme of squares at pH of 14, where the vertical, horizontal, and diagonal arrows indicate PT, ET, and PET reactions, respectively. PT is quantified by pK_a, while ET and PET are assessed by redox potentials (V_{SHE}).

Compound **17**, depicted in Figure 20, is named as ”1,4-dihydroxyanthraquinone” (1,4-DHAQ). During a reduction reaction, it accepts 2 protons and 2 electrons through PET reactions. The reaction is a reversible reaction. The calculated redox potential for the 2PET process is about -0.547 V_{SHE}, whereas the experimental value is measured at -0.539 V_{SHE}.

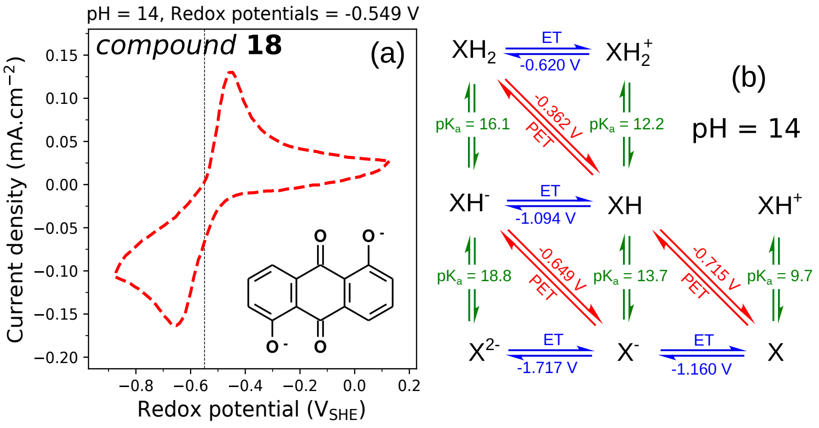

Figure 21: (a) Experimental CV of *compound* **18** accompanied by molecular structure in its oxidized form taken form Ref. [35]. The measured redox potential is indicated by a vertical dashed line. (b) The scheme of squares at pH of 14, where the vertical, horizontal, and diagonal arrows indicate PT, ET, and PET reactions, respectively. PT is quantified by $\mathrm{p}K_\mathrm{a}$, while ET and PET are assessed by redox potentials (V_SHE).

Compound **18**, depicted in Figure 21, is named as ”1,5-dihydroxyanthraquinone” (1,5-DHAQ). During the reduction reaction, it accepts 2 protons and 2 electrons through PET reactions. It undergoes a reversible reaction. The calculated redox potential is -0.539 V_SHE, whereas the experimental value is measured at -0.549 V_SHE.

Compound **19**, depicted in Figure 22, is named as ”benzo[a]phenazine-5-ol” (HBP). The reversible redox reaction occurs through the PET reaction. The standard redox potential for the 2-proton 2-electron transfer (2PET) process is about -0.840 V_SHE, while the experimental value is measured at -0.802 V_SHE. From the scheme of squares, one can see that the ET-PET-PT pathway is also available for redox reactions.

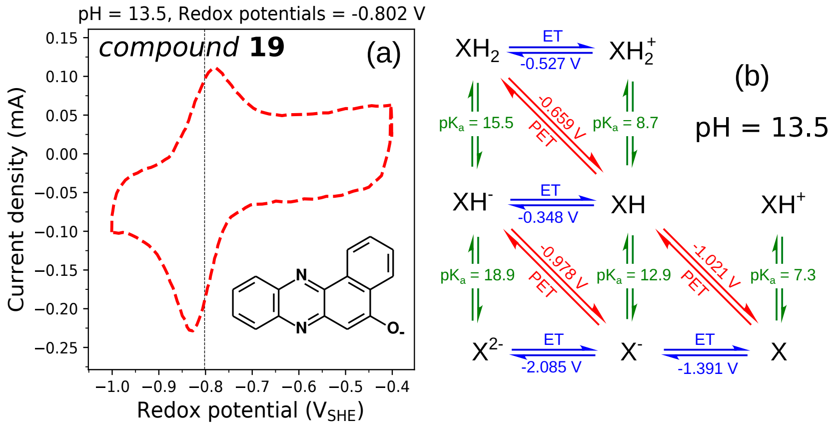

Figure 22: (a) Experimental CV of *compound* **19** accompanied by molecular structure in its oxidized form taken form Ref. [36]. The measured redox potential is indicated by a vertical dashed line. (b) The scheme of squares at pH of 14, where the vertical, horizontal, and diagonal arrows indicate PT, ET, and PET reactions, respectively. PT is quantified by pK_a, while ET and PET are assessed by redox potentials (V_SHE).

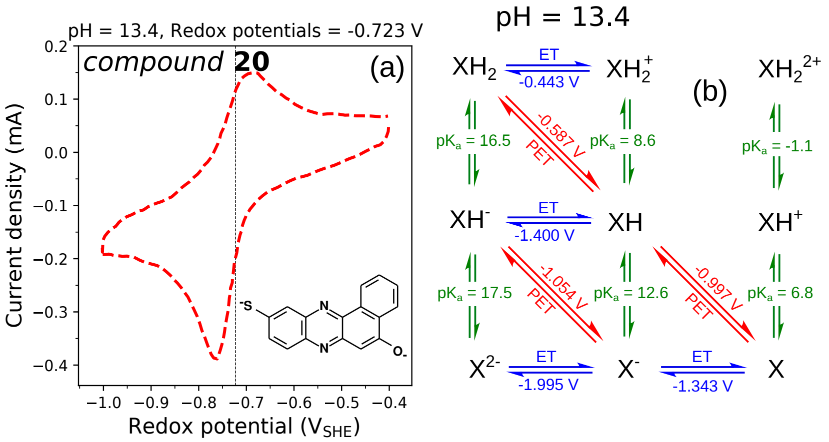

Figure 23: (a) Experimental CV of *compound* **20** accompanied by molecular structure in its oxidized form taken form Ref. [36]. The measured redox potential is indicated by a vertical dashed line. (b) The scheme of squares at pH of 13.4, where the vertical, horizontal, and diagonal arrows indicate PT, ET, and PET reactions, respectively. PT is quantified by pK_a, while ET and PET are assessed by redox potentials (V_SHE).

Compound **20**, illustrated in Figure 23, is named as ”benzo[a]phenazin-5-ol methanesulfonate” (BHPS). During a reduction reaction, the species accepts 2 protons and 2 electrons through PET reactions. The reaction is a reversible redox reaction where the calculated redox potential for the 2PET process is -0.792 V_{SHE}. The experimental value was measured at -0.723 V_{SHE}.

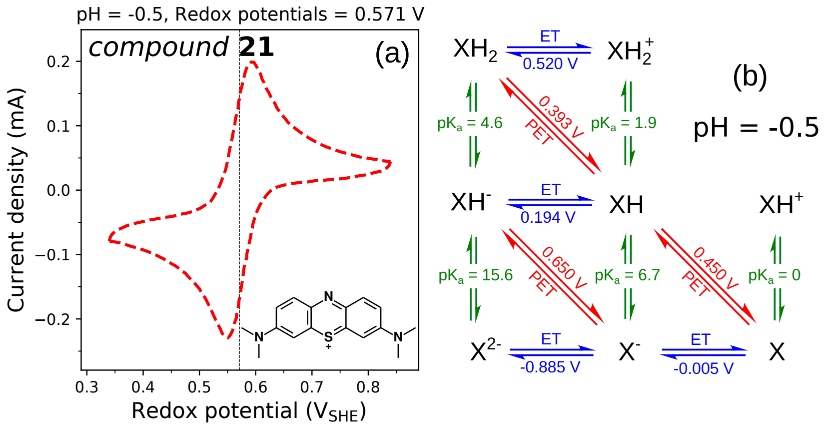

Figure 24: (a) Experimental CV of *compound* **21** accompanied by molecular structure in its oxidized form taken form Ref. [37]. The measured redox potential is indicated by a vertical dashed line. (b) The scheme of squares at pH of -0.5, where the vertical, horizontal, and diagonal arrows indicate PT, ET, and PET reactions, respectively. PT is quantified by $\mathrm{p}K_{\mathrm{a}}$, while ET and PET are assessed by redox potentials (V_{SHE}).

Compound **21**, illustrated in Figure 24, is named as ”methylene blue” (MB). In the reduction reaction, the molecule undergoes two sequential PET reactions. Its reduced form can be reversibly oxidized. In other words, the redox reaction is reversible. The calculated redox potential for these reactions is 0.422 V_{SHE}, while the experimental value is measured at 0.571 V_{SHE}.

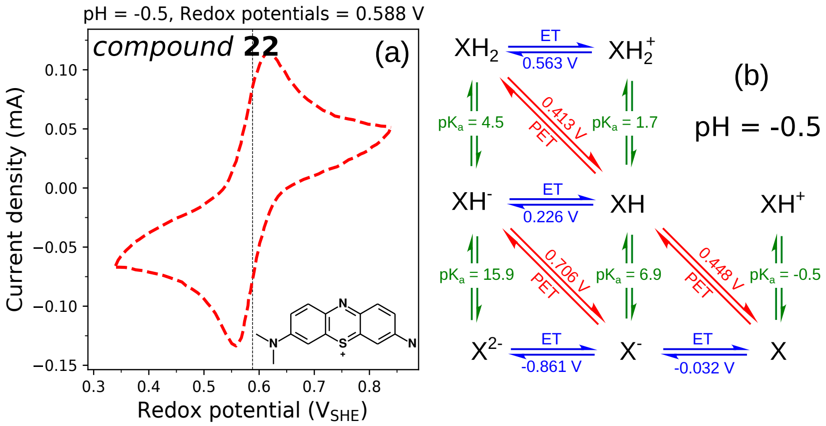

Figure 25: (a) Experimental CV of *compound* **22** accompanied by molecular structure in its oxidized form taken form Ref. [37]. The measured redox potential is indicated by a vertical dashed line. (b) The scheme of squares at pH of -0.5, where the vertical, horizontal, and diagonal arrows indicate PT, ET, and PET reactions, respectively. PT is quantified by $\mathrm{p}K_\mathrm{a}$, while ET and PET are assessed by redox potentials ($\mathrm{V_{SHE}}$).

Compound **22**, depicted in Figure 25, is named as ”Azure A”. During a reduction reaction, It accepts 2 protons and 2 electrons through PET reactions. It undergoes a reversible reaction. The standard redox potential for the 2-proton 2-electron transfer (2PET) process is about 0.422 $\mathrm{V_{SHE}}$, whereas the experimental value is measured at 0.588 $\mathrm{V_{SHE}}$.

Compound **23**, illustrated in Figure 26, is named as ”4,4′-(phenazine-2,3-diylbis(oxy))- dibutyric acid” (2,3-O-DBAP). The molecule X is electrochemically reduced to $\mathrm{XH_2}$ through two PET (2PET) reactions. The $\mathrm{XH_2}$ species can be oxidized back to X through the same pathway. The calculated redox potential for the 2PET process is -0.494 $\mathrm{V_{SHE}}$, compared to the experimental value of -0.641 $\mathrm{V_{SHE}}$.

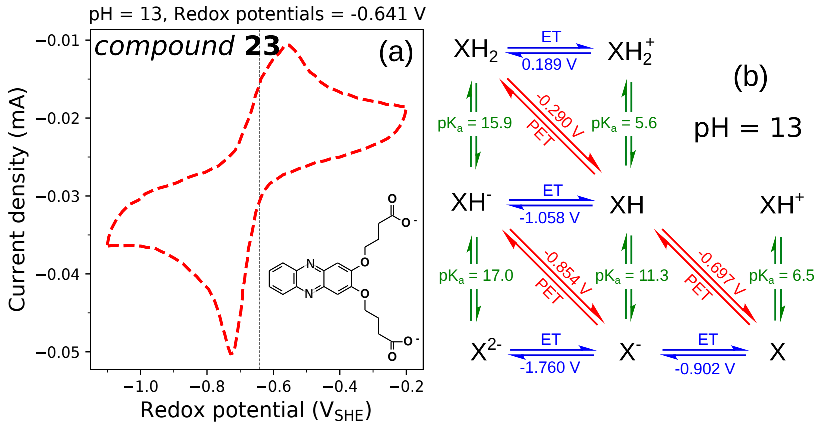

Figure 26: (a) Experimental CV of *compound* **23** accompanied by molecular structure in its oxidized form taken form Ref. [38]. The measured redox potential is indicated by a vertical dashed line. (b) The scheme of squares at pH of 14, where the vertical, horizontal, and diagonal arrows indicate PT, ET, and PET reactions, respectively. PT is quantified by pK_{a}, while ET and PET are assessed by redox potentials (V$_{\mathrm{SHE}}$).

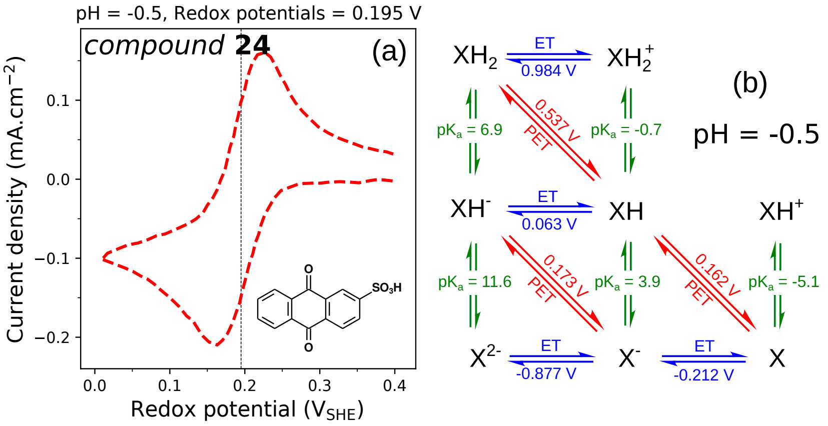

Figure 27: (a) Experimental CV of *compound* **24** accompanied by molecular structure in its oxidized form taken form Ref. [39]. The measured redox potential is indicated by a vertical dashed line. (b) The scheme of squares at pH of -0.5, where the vertical, horizontal, and diagonal arrows indicate PT, ET, and PET reactions, respectively. PT is quantified by pK_{a}, while ET and PET are assessed by redox potentials (V$_{\mathrm{SHE}}$).

Compound **24**, illustrated in Figure 27, is named as ”anthraquinone-2-sulfonic acid” (AQS). In the course of reduction reaction, it accepts 2 protons and 2 electrons through PET reactions. It undergoes a reversible reaction and is oxidized back to X through the same mechanism. The calculated redox potential is 0.349 V_{SHE}, while the experimental value is measured at 0.195 V_{SHE}.

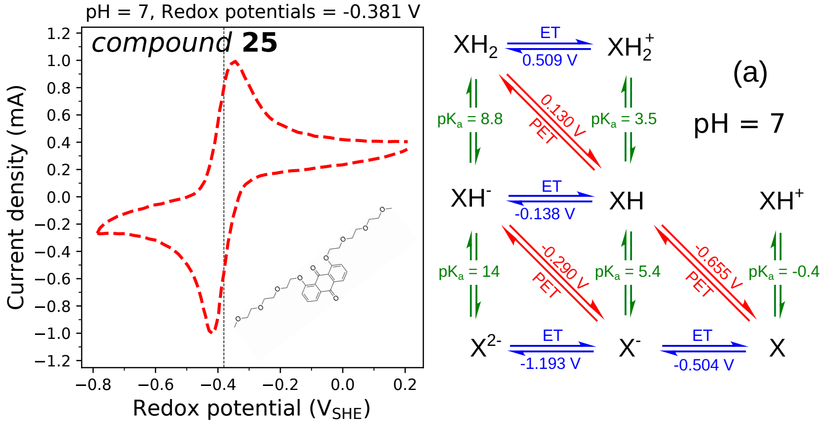

Figure 28: (a) Experimental CV of *compound* **25** accompanied by molecular structure in its oxidized form taken form Ref. [40]. The measured redox potential is indicated by a vertical dashed line. (b) The scheme of squares at pH of 7, where the vertical, horizontal, and diagonal arrows indicate PT, ET, and PET reactions, respectively. PT is quantified by pK_a, while ET and PET are assessed by redox potentials (V_{SHE}).

Compound **25**, depicted in Figure 28, is named as ”1,8-bis(2-(2-(2-methoxyethoxy)ethoxy)ethoxy)anthracene-9,10-dione”. In the reduction reaction, the molecule X accepts 2 protons and 2 electrons through PET reactions. It undergoes a reversible reaction. The calculated redox potential for the 2PET process is -0.263 V_{SHE}, whereas the experimental value is measured at -0.381 V_{SHE}.

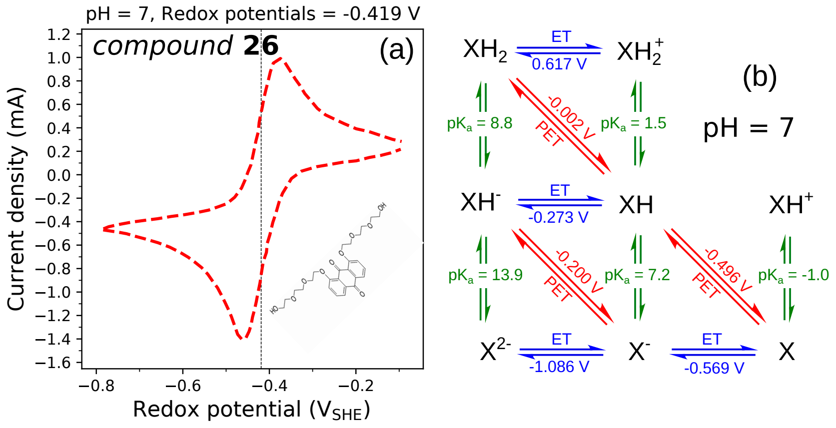

Figure 29: (a) Experimental CV of *compound* **26** accompanied by molecular structure in its oxidized form taken form Ref. [40]. The measured redox potential is indicated by a vertical dashed line. (b) The scheme of squares at pH of 7, where the vertical, horizontal, and diagonal arrows indicate PT, ET, and PET reactions, respectively. PT is quantified by pK_a, while ET and PET are assessed by redox potentials ($\mathrm{V_{SHE}}$).

Compound **26**, depicted in Figure 29, is named as ”1,8-bis(2-(2-(2-hydroxyethoxy)ethoxy)ethoxy)anthracene-9,10-dione”. During the reduction reaction, molecule X is converted into XH and subsequently into XH_2 through the PET pathways. The redox potential for the reversible 2PET process is -0.249 $\mathrm{V_{SHE}}$, while the experimental value is measured at -0.419 $\mathrm{V_{SHE}}$.

Compound **27**, depicted in Figure 30, is named as ”lumichrome”. During the reduction reaction, it accepts two protons and two electrons through PET reactions. This process is reversible. The calculated redox potential for the 2PET process is -0.856 $\mathrm{V_{SHE}}$, while the experimental value is measured at -0.685 $\mathrm{V_{SHE}}$.

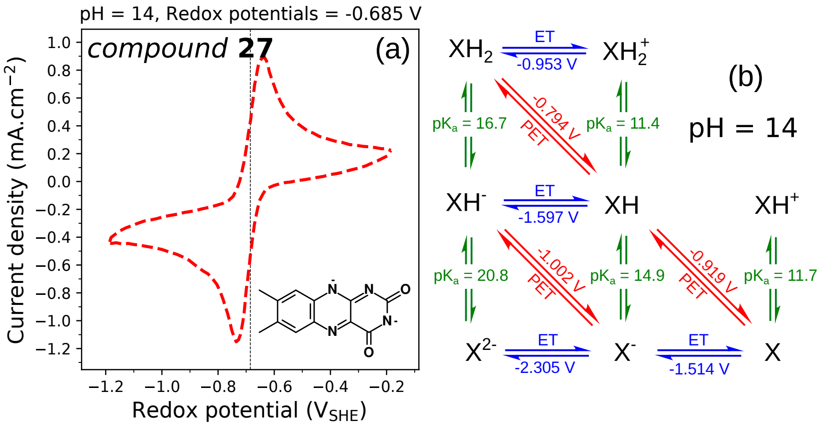

Figure 30: (a) Experimental CV of *compound* **27** accompanied by molecular structure in its oxidized form taken form Ref. [32]. The measured redox potential is indicated by a vertical dashed line. (b) The scheme of squares at pH of 14, where the vertical, horizontal, and diagonal arrows indicate PT, ET, and PET reactions, respectively. PT is quantified by pK_a, while ET and PET are assessed by redox potentials (V$_\mathrm{SHE}$).

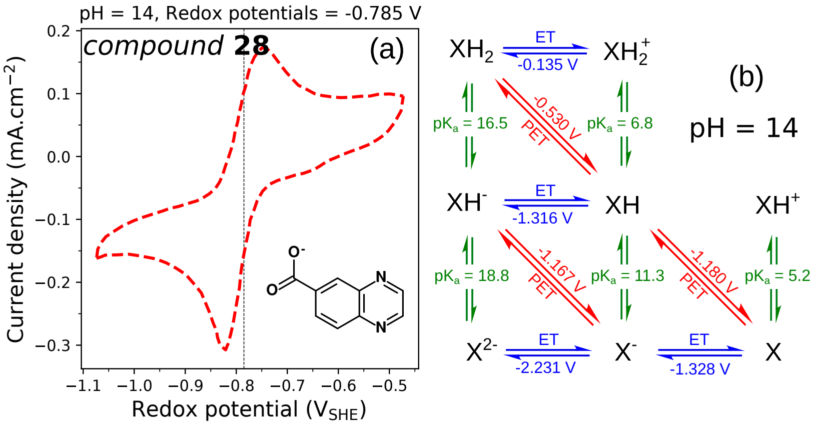

Figure 31: (a) Experimental CV of *compound* **28** accompanied by molecular structure in its oxidized form taken form Ref. [41]. The measured redox potential is indicated by a vertical dashed line. (b) The scheme of squares at pH of 14, where the vertical, horizontal, and diagonal arrows indicate PT, ET, and PET reactions, respectively. PT is quantified by pK_a, while ET and PET are assessed by redox potentials (V$_\mathrm{SHE}$).

Compound **28**, depicted in Figure 31, is named as ”6-quinoxalinecarboxylic acid” (QCA). QCA in its X form participates in two sequential PET reactions, ultimately forming XH$_2$. The final reduced species can be oxidized back to X through the same reaction pathways, indicating that it is a reversible reaction. The calculated redox potential for this 2PET process is -0.855 V_{SHE}, whereas the experimental value is measured at -0.785 V_{SHE}.

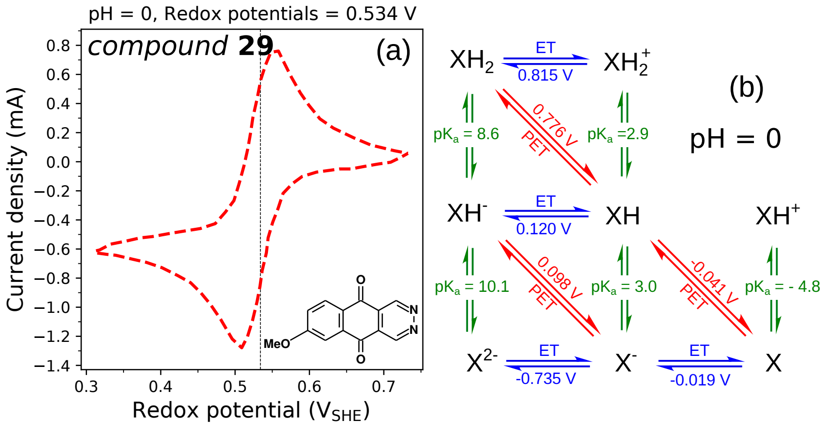

Figure 32: (a) Experimental CV of *compound* **29** accompanied by molecular structure in its oxidized form taken form Ref. [33]. The measured redox potential is indicated by a vertical dashed line. (b) The scheme of squares at pH of 0, where the vertical, horizontal, and diagonal arrows indicate PT, ET, and PET reactions, respectively. PT is quantified by pK_a, while ET and PET are assessed by redox potentials (V_{SHE}).

Compound **29**, depicted in Figure 32, is named as ”2,3-diaza-6-methoxy-anthracene-9,10-dione” (DAD(MeO)). During the reduction reaction, it accepts 2 protons and 2 electrons through PET reactions. It undergoes a reversible reaction to oxidize back. The calculated redox potential for the 2PET process is 0.292 V_{SHE}, while the experimental value is measured at 0.534 V_{SHE}.

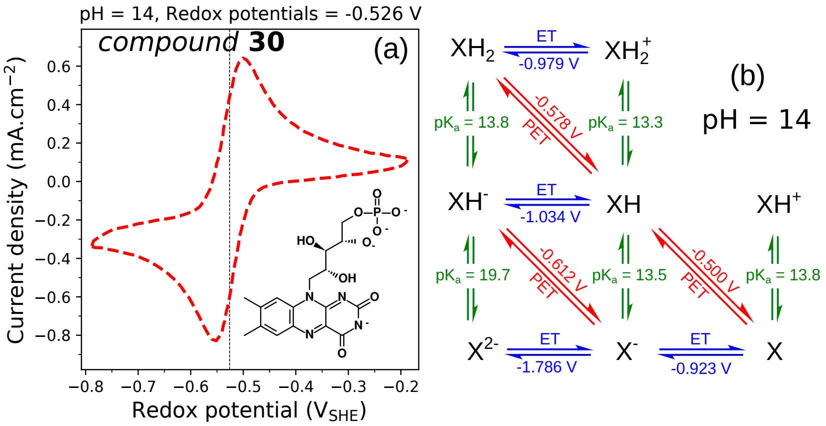

Figure 33: (a) Experimental CV of *compound* **30** accompanied by molecular structure in its oxidized form taken form Ref. [32]. The measured redox potential is indicated by a vertical dashed line. (b) The scheme of squares at pH of 14, where the vertical, horizontal, and diagonal arrows indicate PT, ET, and PET reactions, respectively. PT is quantified by pK_a, while ET and PET are assessed by redox potentials ($\mathrm{V_{SHE}}$).

Compound **30**, depicted in Figure 33, is named as ”riboflavin-5-phosphate” (FMN). In a reduction process, it accepts 2 protons and 2 electrons through PET reactions. The fully reduced species (XH_2) can be reversibly oxidized back to X. It is worth mentioning that a pK_a of 13.8 indicates an equilibrium between XH_2 and XH^- at a pH of 14. This means that XH_2 will be sufficiently present for the oxidation reaction. The calculated redox potential is -0.539 $\mathrm{V_{SHE}}$, compared to the experimental value of -0.526 $\mathrm{V_{SHE}}$.

Compound **31**, *N,N,N’,N’-tetramethyl-[1,1’-biphenyl]-4,4’-diamine* (TMB), is depicted in Figure 34. In a reduction reaction, TMB accepts 2 protons and 2 electrons through the ET-PT-PET reactions. Indeed, 2PET might also be highly probable due to the low pH environment. It undergoes a reversible reaction where oxidation only occurs through PET reactions. The redox potential for the these redox reactions is 0.917 $\mathrm{V_{SHE}}$, whereas the experimental value is measured at 0.785 $\mathrm{V_{SHE}}$.

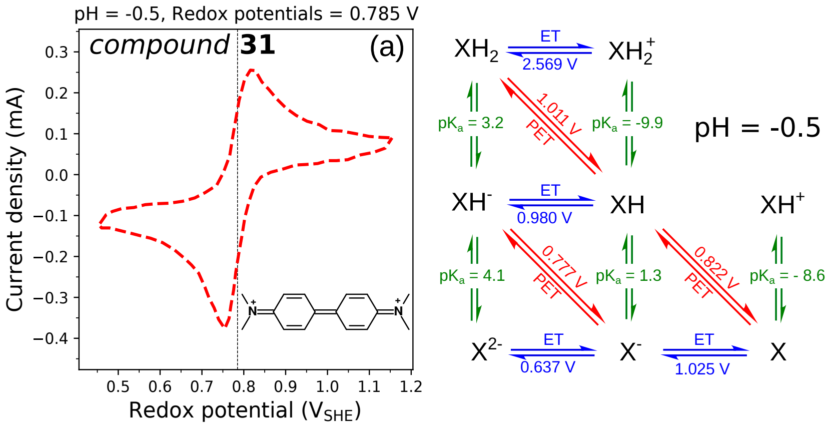

Figure 34: (a) Experimental CV of *compound* **31** accompanied by molecular structure in its oxidized form taken form Ref. [42]. The measured redox potential is indicated by a vertical dashed line. (b) The scheme of squares at pH of -0.5, where the vertical, horizontal, and diagonal arrows indicate PT, ET, and PET reactions, respectively. PT is quantified by pK_a, while ET and PET are assessed by redox potentials ($\mathrm{V_{SHE}}$).

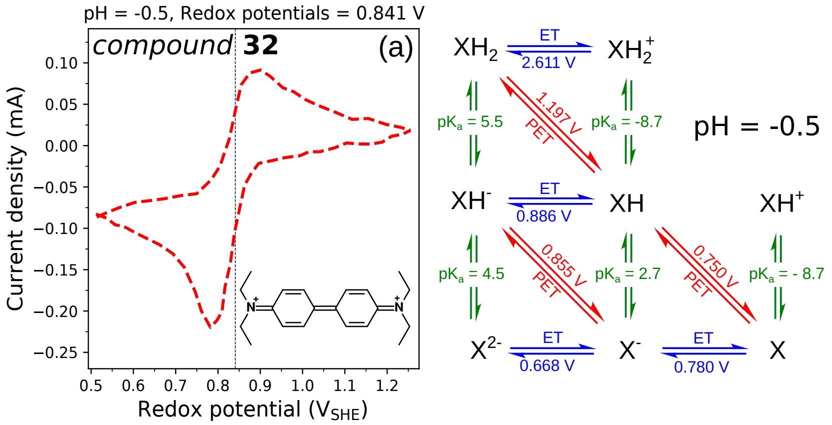

Figure 35: (a) Experimental CV of *compound* **32** accompanied by molecular structure in its oxidized form taken form Ref. [42]. The measured redox potential is indicated by a vertical dashed line. (b) The scheme of squares at pH of -0.5, where the vertical, horizontal, and diagonal arrows indicate PT, ET, and PET reactions, respectively. PT is quantified by pK_a, while ET and PET are assessed by redox potentials ($\mathrm{V_{SHE}}$).

Compound **32**, *N,N,N',N'-tetraethyl-[1,1'-biphenyl]-4,4'-diamine* (TEB), is depicted in Figure 35. In a reduction reaction, TEB accepts 2 protons and 2 electrons through ET-PET-PT reactions. Indeed, 2PET might also be highly probable due to the low pH environment. It undergoes a reversible reaction where oxidation only occurs through PET reactions. The redox potential for the these redox reactions is 0.974 V_{SHE}, whereas the experimental value is measured at 0.841 V_{SHE}.

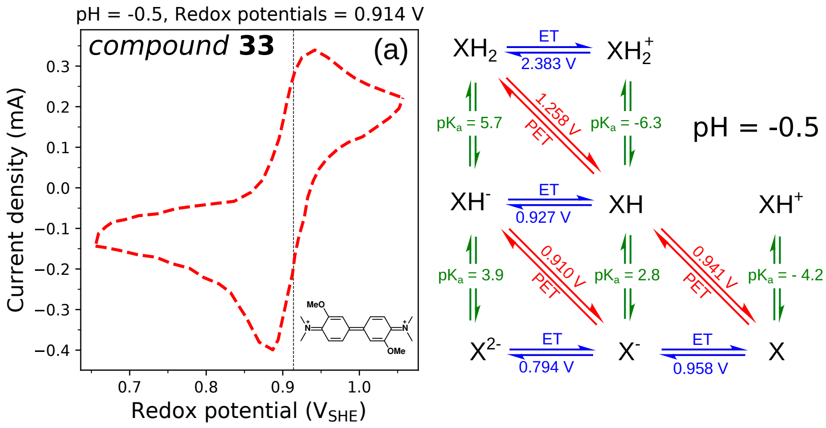

Figure 36: (a) Experimental CV of *compound* **33** accompanied by molecular structure in its oxidized form taken form Ref. [42]. The measured redox potential is indicated by a vertical dashed line. (b) The scheme of squares at pH of -0.5, where the vertical, horizontal, and diagonal arrows indicate PT, ET, and PET reactions, respectively. PT is quantified by $\mathrm{p}K_{\mathrm{a}}$, while ET and PET are assessed by redox potentials (V_{SHE}).

Compound **33**, *3,3'-dimethoxy-N,N,N',N'-tetramethyl-[1,1'-biphenyl]-4,4'-diamine* (o-DMOTMB), is depicted in Figure 36. In a reduction reaction, o-DMOTMB accepts 2 protons and 2 electrons through sequential PET reactions. It undergoes a reversible reaction where oxidation only occurs through PET reactions. The redox potential for the these redox reactions is 1.099 V_{SHE}, whereas the experimental value is measured at 0.914 V_{SHE}.

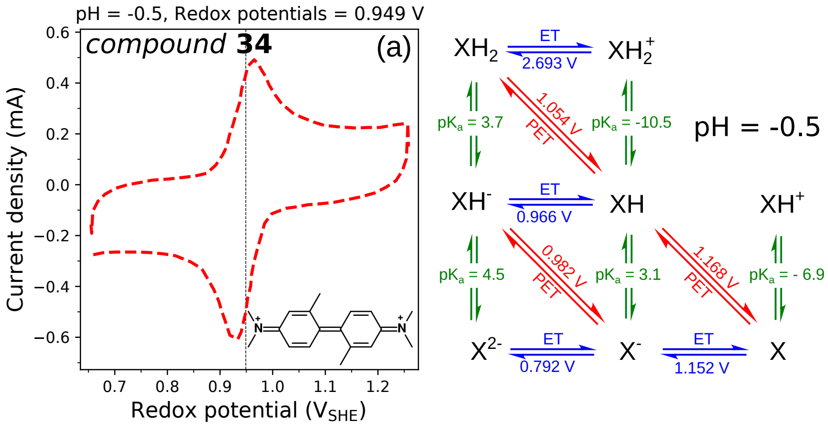

Figure 37: (a) Experimental CV of *compound* **34** accompanied by molecular structure in its oxidized form taken form Ref. [42]. The measured redox potential is indicated by a vertical dashed line. (b) The scheme of squares at pH of -0.5, where the vertical, horizontal, and diagonal arrows indicate PT, ET, and PET reactions, respectively. PT is quantified by pK_a, while ET and PET are assessed by redox potentials ($\mathrm{V_{SHE}}$).

Compound **34**, *3N,N,N',N',2,2'-hexamethyl-[1,1'-biphenyl]-4,4'-diamine* (m-DMTMB), is depicted in Figure 37. In a reduction reaction, m-DMTMB accepts 2 protons and 2 electrons through either sequential PET reactions (2PET). It undergoes a reversible reaction where oxidation only occurs through PET reactions. The redox potential for the these redox reactions is 1.111 $\mathrm{V_{SHE}}$, whereas the experimental value is measured at 0.949 $\mathrm{V_{SHE}}$.

Compound **35**, *(4,4'-bis(dimethylamino)-[1,1'-biphenyl]-2,2'-diyl)dimethanol* (m-DHMTMB), is depicted in Figure 38. In a reduction reaction, m-DHMTMB accepts 2 protons and 2 electrons through sequential PET reactions (2PET). It undergoes a reversible reaction where oxidation only occurs through PET reactions. The redox potential for the these redox reactions is 1.171 $\mathrm{V_{SHE}}$, whereas the experimental value is measured at 0.990 $\mathrm{V_{SHE}}$. Note that even if the ET reaction for X is energetically more favorable, it is still outside the range of the applied potential.

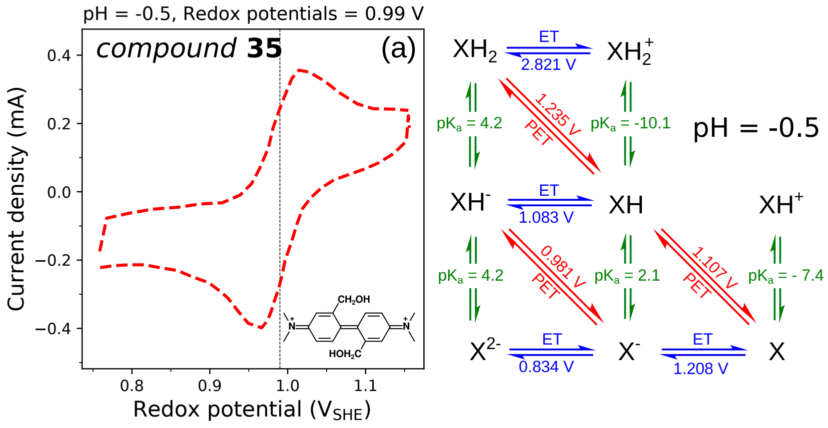

Figure 38: (a) Experimental CV of *compound* **35** accompanied by molecular structure in its oxidized form taken form Ref. [42]. The measured redox potential is indicated by a vertical dashed line. (b) The scheme of squares at pH of -0.5, where the vertical, horizontal, and diagonal arrows indicate PT, ET, and PET reactions, respectively. PT is quantified by pK_a, while ET and PET are assessed by redox potentials ($\mathrm{V_{SHE}}$).

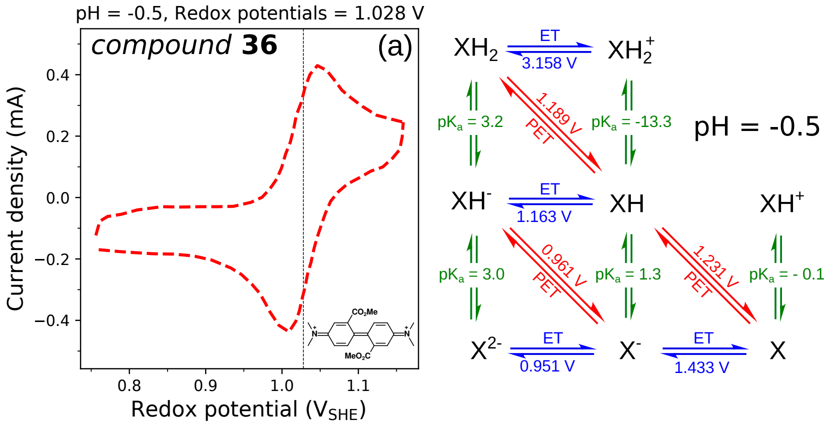

Figure 39: (a) Experimental CV of *compound* **36** accompanied by molecular structure in its oxidized form taken form Ref. [42]. The measured redox potential is indicated by a vertical dashed line. (b) The scheme of squares at pH of -0.5, where the vertical, horizontal, and diagonal arrows indicate PT, ET, and PET reactions, respectively. PT is quantified by pK_a, while ET and PET are assessed by redox potentials ($\mathrm{V_{SHE}}$).

Compound **36**, *Dimethyl 4,4'-bis(dimethylamino)-[1,1'-biphenyl]-2,2'-dicarboxylate* (m-DMOCTMB), is depicted in Figure 39. In a reduction reaction, m-DMOCTMB accepts 2 protons and 2 electrons through sequential PET reactions

(2PET). It undergoes a reversible redox reaction where oxidation only occurs through 2PET pathway. The redox potential for the these redox reactions is 1.210 $\mathrm{V_{SHE}}$, whereas the experimental value is measured at 1.028 $\mathrm{V_{SHE}}$. It is worth mentioning that even if the ET reaction for X is energetically more favorable, it is still outside the range of the applied potential.

7. Examples of Irreversible Proton-Electron Transfer Reactions

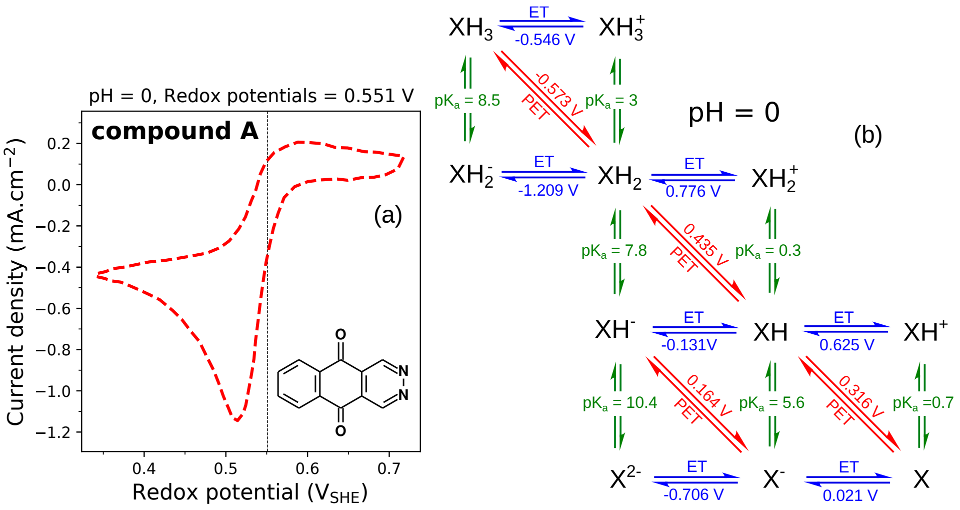

Figure 40: (a) Experimental CV of **compound A** accompanied by molecular structure in its oxidized form taken form Ref. [33]. The measured redox potential is indicated by a vertical dashed line. (b) The scheme of squares at pH of 0, where the vertical, horizontal, and diagonal arrows indicate PT, ET, and PET reactions, respectively. PT is quantified by pK_a, while ET and PET are assessed by redox potentials ($\mathrm{V_{SHE}}$).

Compound A, depicted in Figure 40, is named as ”3-diaza-9,10-anthracenedione” (DAD). Similar to many cases illustrated in Section 6, **Compound A** undergoes a 2PET reaction and forms $\mathrm{XH_2}$. To discover the next step, let us have a look at $\mathrm{XH_3^+}$. At this stage, because the pK_a of molecule $\mathrm{XH_3^+}$ is higher than the pH of the solution, $\mathrm{XH_3^+}$ cannot deprotonate to form $\mathrm{XH_2}$. Instead, $\mathrm{XH_2}$ will immediately protonate to form $\mathrm{XH_3^+}$. The final species, $\mathrm{XH_3^+}$, will remain stable and will not be oxidized under any conditions.

Compound B, depicted in Figure 41, is named as ”2,3-diaza-5,8-dihydroxy-anthracene-9,10-dione” DADdi(OH). **Compound B** undergoes the same mechanism as **Compound A**. To extend our discussion from **Compound A**, we address why $\mathrm{XH_2}$ is not reduced through either ET or PET and is instead protonated. Both reactions, ET and PET, require a significantly higher applied potential, which usually takes some time to achieve. In contrast, in a very acidic solution, protons are highly concentrated and readily available almost everywhere. This accessibility facilitates the protonation of $\mathrm{XH_2}$ over further reduction.

Compound C, depicted in Figure 42, is named as ”1,4-bis(2-(2-(2-hydroxyethoxy)ethoxy)ethoxy)anthracene-9,10-dione”. During a reduction re-

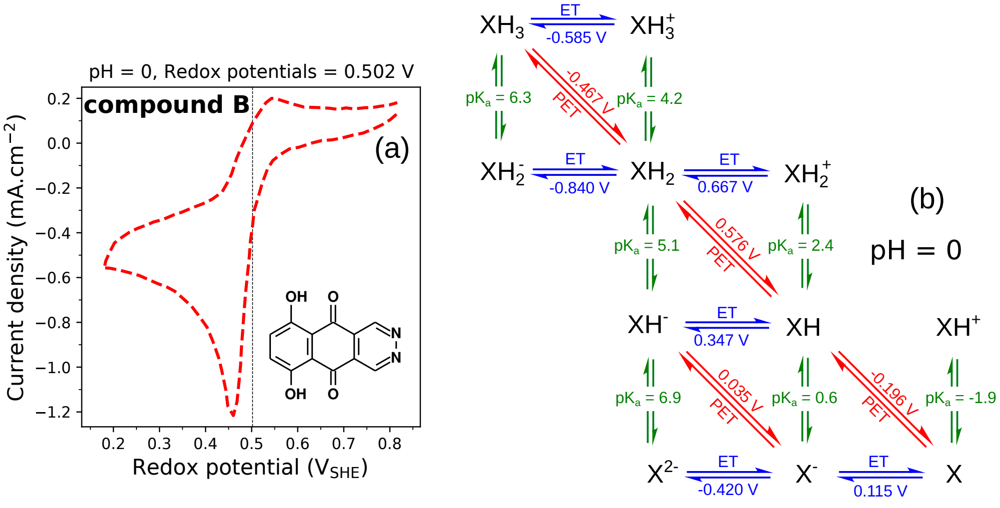

Figure 41: (a) Experimental CV of **compound B** accompanied by molecular structure in its oxidized form taken form Ref. [33]. The measured redox potential is indicated by a vertical dashed line. (b) The scheme of squares at pH of 0, where the vertical, horizontal, and diagonal arrows indicate PT, ET, and PET reactions, respectively. PT is quantified by pK_a, while ET and PET are assessed by redox potentials (V_{SHE}).

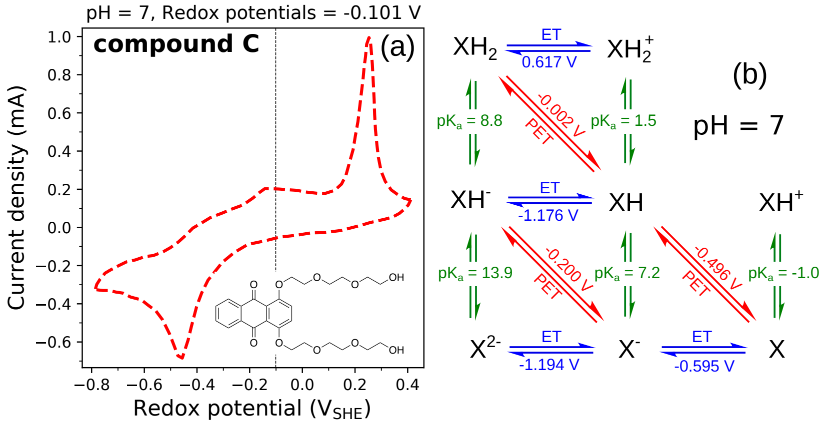

Figure 42: (a) Experimental cyclic voltammetry of the compound at the same pH accompanied by molecular structure in the fully oxidized taken form [40]. (b) The Scheme of Squares of the **compound C** at pH of 7, where the vertical, horizontal, and diagonal arrows indicate PT, ET, and PET reactions, respectively. PT is quantified by pK_a, while ET and PET are assessed by redox potential in V_{SHE}. The formal redox potential is shown by a vertical dashed line.

action, It accepts 1 protons and1 electrons through PET reactions. Due to the varying potentials between the anodic and cathodic reactions. The scheme of squares predicts a pathway that its potential is consistent with experiemntal value during reduction reaction. While, oxidation reactions do not follow the same reaction pathways. Functional group decomposition as a side reaction is highly possible that is out the scope of our investigations.

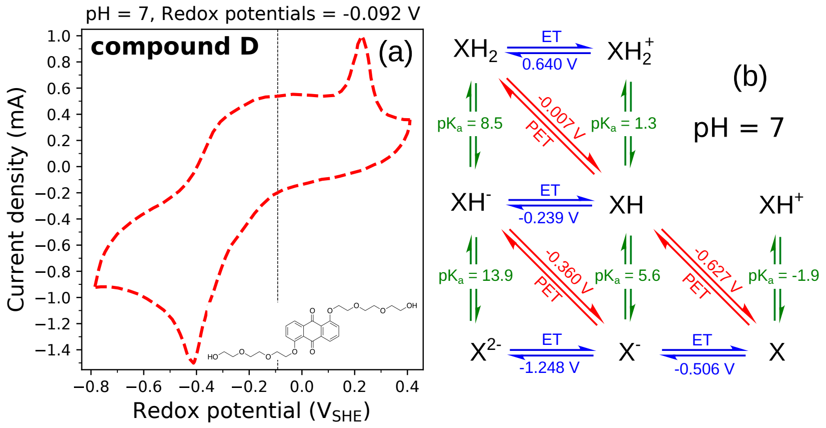

Figure 43: (a) Experimental cyclic voltammetry of the compound at the same pH accompanied by molecular structure in the fully oxidized taken form [40]. (b) The Scheme of Squares of the **compound D** at pH of 7, where the vertical, horizontal, and diagonal arrows indicate PT, ET, and PET reactions, respectively. PT is quantified by pK_a, while ET and PET are assessed by redox potential in V_{SHE}. The formal redox potential is shown by a vertical dashed line.

Compound 5, depicted in Figure 43, is named as ”1,5-bis(2-(2-(2-hydroxyethoxy)ethoxy)ethoxy)anthracene-9,10-dione”. During a reduction reaction, It accepts 1 protons and1 electrons through PET reactions. Due to the varying potentials between the anodic and cathodic reactions, these molecules are irreversible. The scheme of squares predicts a pathway that its potential is consistent with experiemntal value during reduction reaction. While, oxidation reactions do not follow the same reaction pathways. Functional group decomposition as a side reaction is highly possible that is out the scope of our investigations.

8. Discrepancies Between Experimental and Computational cases

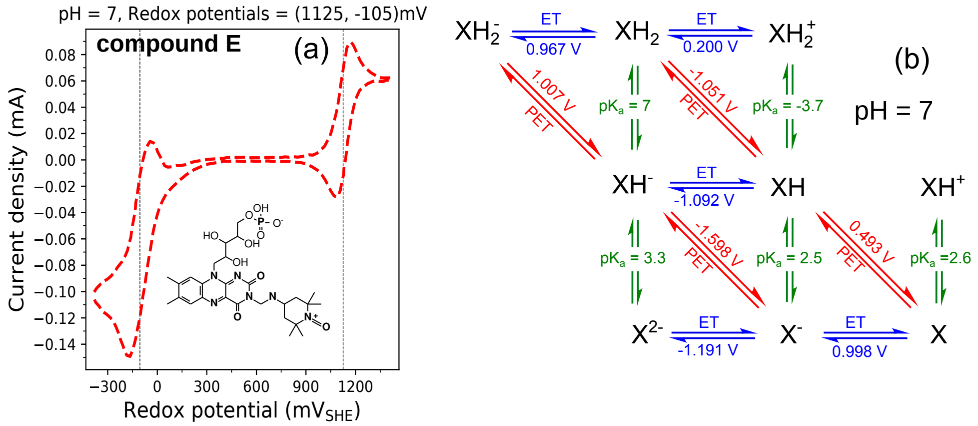

Figure 44: (a) Experimental cyclic voltammetry of the compound at the same pH accompanied by molecular structure in the fully oxidized taken form [43]. (b) The Scheme of Squares of the **compound E** at pH of 7, where the vertical, horizontal, and diagonal arrows indicate PT, ET, and PET reactions, respectively. PT is quantified by pK_a, while ET and PET are assessed by redox potential in V_SHE. The formal redox potential is shown by a vertical dashed line.

Compound E, shown in Figure 44, is named ”iboflavin-TEMPO (RIBOTEMPO)”. During the reduction reaction, it accepts one electron via an ET reaction at a potential of 0.998 V_SHE. A closely matching experimental value of 1.125 V_SHE was measured, attributed to the radical formation of the TEMPO derivative. Referring back to Eq. 9, a second PET reaction can occur at -0.295 V_SHE, which closely aligns with the experimental value of -0.105 V_SHE. However, due to the significantly large value of the first PET (X^--to-XH^-), we have opted to exclude this example from the dataset.

Compound F, depicted in Figure 45, is named ”TEMPO-Viologen”. During the reduction reaction, it accepts one electron through an ET reaction. As experimentally discovered, it subsequently accepts one proton and one electron through PET reactions, followed by accepting another electron through ET. It undergoes a reversible reaction. The computed redox potentials for these reactions are 1.165 V_SHE, 0.069 V_SHE, and -0.418 V_SHE, respectively, whereas the experimental values are measured at 0.973 V_SHE, -0.339 V_SHE, and -0.712 V_SHE. There is a significant deviation between the experimental and computational values for the second and third peaks; therefore, we have also excluded this example from the dataset.

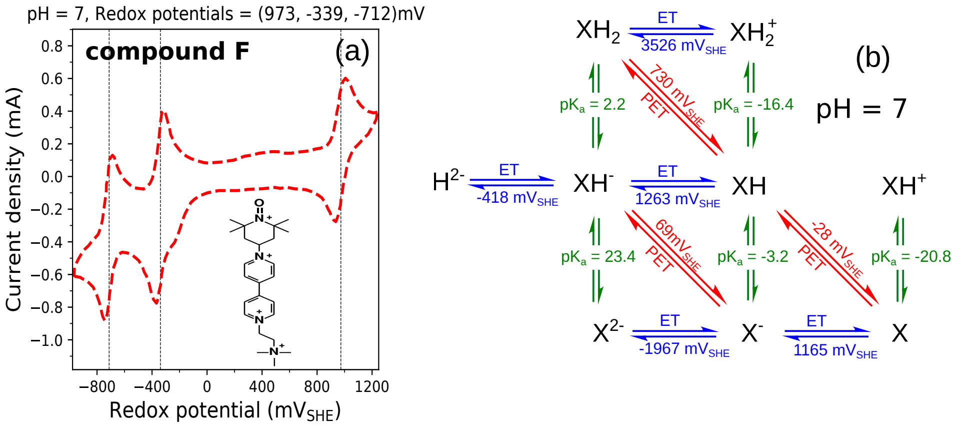

Figure 45: (a) Experimental cyclic voltammetry of the compound at the same pH accompanied by molecular structure in the fully oxidized taken form [20]. (b) The Scheme of Squares of the **compound F** at pH of 7, where the vertical, horizontal, and diagonal arrows indicate PT, ET, and PET reactions, respectively. PT is quantified by pK_a, while ET and PET are assessed by redox potential in V_{SHE}. The formal redox potential is shown by a vertical dashed line.

References

[1] W. Li, J. Li, X. Yuan, Z. Xiang, Z. Liang, and Z. Fu, “A novel pyridinium-functionalized fluorenone compound for neutral aqueous organic redox flow batteries”, J. Mater. Chem. A **11**, 19308–19311 (2023).

[2] C. Caianiello, L. F. Arenas, T. Turek, and R. Wilhelm, “A hydroxylated tetracationic viologen based on dimethylaminoethanol as a negolyte for aqueous flow batteries”, Batteries & Supercaps **6**, e202200355 (2023).

[3] J. Rodriguez, C. Niemet, and L. D. Pozzo, “Fluorenone based anolyte for an aqueous organic redox-flow battery”, ECS Transactions **89**, 49 (2019).

[4] Y. Liu, M.-A. Goulet, L. Tong, Y. Liu, Y. Ji, L. Wu, R. G. Gordon, M. J. Aziz, Z. Yang, and T. Xu, “A long-lifetime all-organic aqueous flow battery utilizing tmap-tempo radical”, Chem **5**, 1861–1870 (2019).

[5] T. Liu, X. Wei, Z. Nie, V. Sprenkle, and W. Wang, “A total organic aqueous redox flow battery employing a low cost and sustainable methyl viologen anolyte and 4-ho-tempo catholyte”, Advanced Energy Materials **6**, 1501449 (2016).

[6] H. Li, H. Fan, B. Hu, L. Hu, G. Chang, and J. Song, “Spatial structure regulation: a rod-shaped viologen enables long lifetime in aqueous redox flow batteries”, Angewandte Chemie International Edition **60**, 26971–26977 (2021).

[7]B. Hu, M. Hu, J. Luo, and T. L. Liu, "A stable, low permeable tempo catholyte for aqueous total organic redox flow batteries", Advanced Energy Materials **12**, 2102577 (2022).

[8]J. Luo, B. Hu, C. Debruler, and T. L. Liu, "A -conjugation extended viologen as a two-electron storage anolyte for total organic aqueous redox flow batteries", Angewandte Chemie International Edition **57**, 231–235 (2018).

[9]S. de la Parra, J. A. Tamayo-Ramos, R. Rubio-Presa, D. Perez-Antolin, V. Ruiz, R. Sanz, C. Rumbo, and E. Ventosa, "On the tunability of toxicity for viologen-derivatives as anolyte for neutral aqueous organic redox flow batteries", ChemSusChem **16**, e202300626 (2023).

[10]S. Jin, E. M. Fell, L. Vina-Lopez, Y. Jing, P. W. Michalak, R. G. Gordon, and M. J. Aziz, "Near neutral ph redox flow battery with low permeability and long-lifetime phosphonated viologen active species", Advanced Energy Materials **10**, 2000100 (2020).

[11]Y. Liu, Y. Li, P. Zuo, Q. Chen, G. Tang, P. Sun, Z. Yang, and T. Xu, "Screening viologen derivatives for neutral aqueous organic redox flow batteries", ChemSusChem **13**, 2245–2249 (2020).

[12]M. Pan, L. Gao, J. Liang, P. Zhang, S. Lu, Y. Lu, J. Ma, and Z. Jin, "Reversible redox chemistry in pyrrolidinium-based tempo radical and extended viologen for high-voltage and long-life aqueous redox flow batteries", Advanced Energy Materials **12**, 2103478 (2022).

[13]B. Ambrose, R. P. Naresh, M. Ulaganathan, P. Ragupathy, and M. Kathiresan, "Modified viologen as an efficient anolyte for aqueous organic redox flow batteries", Materials Letters **314**, 131876 (2022).

[14]C. DeBruler, B. Hu, J. Moss, X. Liu, J. Luo, Y. Sun, and T. L. Liu, "Designer two-electron storage viologen anolyte materials for neutral aqueous organic redox flow batteries", Chem **3**, 961–978 (2017).

[15]G. Tang, Y. Liu, Y. Li, K. Peng, P. Zuo, Z. Yang, and T. Xu, "Designing robust two-electron storage extended bipyridinium anolytes for ph-neutral aqueous organic redox flow batteries", JACS Au **2**, 1214–1222 (2022).

[16]X.-L. Lv, P. Sullivan, H.-C. Fu, X. Hu, H. Liu, S. Jin, W. Li, and D. Feng, "Dextrosil-viologen: a robust and sustainable anolyte for aqueous organic redox flow batteries", ACS Energy Letters **7**, 2428–2434 (2022).

[17] P. T. Sullivan, H. Liu, X.-L. Lv, S. Jin, W. Li, and D. Feng, "Viologen hydrothermal synthesis and structure–property relationships for redox flow battery optimization", Advanced Energy Materials **13**, 2203919 (2023).

[18] E. Pedraza, C. de la Cruz, A. Mavrandonakis, E. Ventosa, R. Rubio-Presa, R. Sanz, S. T. Senthilkumar, P. Navalpotro, and R. Marcilla, "Unprecedented aqueous solubility of tempo and its application as high capacity catholyte for aqueous organic redox flow batteries", Advanced Energy Materials **13**, 2301929 (2023).

[19] X. Zhang, X. Liu, H. Zhang, Z. Wang, Y. Zhang, G. Li, M.-j. Li, and G. He, "Robust chalcogenophene viologens as anolytes for long-life aqueous organic redox flow batteries with high battery voltage", ACS Applied Materials & Interfaces **14**, 48727–48733 (2022).

[20] L. Wang, M. Huang, K. Wan, Z. Fu, Z. Xiang, and Z. Liang, "Highly soluble tempo-viologen bipolar molecule for ultra-stable aqueous redox flow batteries", Advanced Functional Materials **34**, 2310620 (2024).

[21] K. Amini, E. F. Kerr, T. Y. George, A. M. Alfaraidi, Y. Jing, T. Tsukamoto, R. G. Gordon, and M. J. Aziz, "An extremely stable, highly soluble monosubstituted anthraquinone for aqueous redox flow batteries", Advanced Functional Materials **33**, 2211338 (2023).

[22] A. M. Alfaraidi, D. Xi, N. Ni, T. Y. George, T. Tsukamoto, R. G. Gordon, M. J. Aziz, and R. Y. Liu, "An extremely stable and soluble nh2-substituted anthraquinone electrolyte for aqueous redox flow batteries", ACS Applied Energy Materials **6**, 12259–12266 (2023).

[23] E. F. Kerr, Z. Tang, T. Y. George, S. Jin, E. M. Fell, K. Amini, Y. Jing, M. Wu, R. G. Gordon, and M. J. Aziz, "High energy density aqueous flow battery utilizing extremely stable, branching-induced high-solubility anthraquinone near neutral ph", ACS Energy Letters **8**, `10.1021/acsenergylett.2c01691` (2022).

[24] H. Fan et al., "Radical charge population and energy: critical role in redox potential and cycling life of piperidine nitroxyl radical cathodes in aqueous zinc hybrid flow batteries", ACS Applied Materials & Interfaces **12**, 43568–43575 (2020).

[25] M. Gao, M. Salla, Y. Song, and Q. Wang, "High-power near-neutral aqueous all organic redox flow battery enabled with a pair of anionic redox species", Angewandte Chemie International Edition **61**, e202208223 (2022).

[26]B. Hu, H. Fan, H. Li, M. Ravivarma, and J. Song, “Five-membered ring nitroxide radical: a new class of high-potential, stable catholytes for neutral aqueous organic redox flow batteries”, Advanced Functional Materials **31**, 2102734 (2021).

[27]Y. Liu, Q. Chen, P. Sun, Y. Li, Z. Yang, and T. Xu, “Organic electrolytes for aqueous organic flow batteries”, Materials Today Energy **20**, 100634 (2021).

[28]L. Xia, W. Huo, H. Gao, H. Zhang, F. Chu, H. Liu, and Z. Tan, “Intramolecular hydrogen bonds induced high solubility for efficient and stable anthraquinone based neutral aqueous organic redox flow batteries”, Journal of Power Sources **498**, 229896 (2021).

[29]Q. Liu, X. Li, C. Yan, and A. Tang, “A dopamine-based high redox potential catholyte for aqueous organic redox flow battery”, Journal of Power Sources **460**, 228124 (2020).

[30]J. D. Hofmann, S. Schmalisch, S. Schwan, L. Hong, H. A. Wegner, D. Mollenhauer, J. Janek, and D. Schröder, “Tailoring dihydroxyphthalazines to enable their stable and efficient use in the catholyte of aqueous redox flow batteries”, Chemistry of Materials **32**, 3427–3438 (2020).

[31]J. Xu, S. Pang, X. Wang, P. Wang, and Y. Ji, “Ultrastable aqueous phenazine flow batteries with high capacity operated at elevated temperatures”, Joule **5**, 2437–2449 (2021).

[32]K. Lin, R. Gómez-Bombarelli, E. S. Beh, L. Tong, Q. Chen, A. Valle, A. Aspuru-Guzik, M. J. Aziz, and R. G. Gordon, “A redox-flow battery with an alloxazine-based organic electrolyte”, Nature Energy **1**, 16102 (2016).

[33]J. D. Hofmann, F. L. Pfanschilling, N. Krawczyk, P. Geigle, L. Hong, S. Schmalisch, H. A. Wegner, D. Mollenhauer, J. Janek, and D. Schröder, “Quest for organic active materials for redox flow batteries: 2,3-diaza-anthraquinones and their electrochemical properties”, Chemistry of Materials **30**, 762–774 (2018).

[34]L. Xu, Q. Wang, D. Guo, J. Xu, and J. Cao, “A quaternized anthraquinone derivative for ph-neutral aqueous organic redox flow batteries”, New J. Chem. **47**, 11216–11221 (2023).

[35]J. Cao, M. Tao, H. Chen, J. Xu, and Z. Chen, “A highly reversible anthraquinone-based anolyte for alkaline aqueous redox flow batteries”, Journal of Power Sources **386**, 40–46 (2018).

[36] J. Park, Y. Lee, D. Yun, D. Kim, G. Hwang, B. Han, Y. Kim, J. Jung, and J. Jeon, "A benzo[a]phenazine-based redox species with highly reversible two-electron reaction for aqueous organic redox flow batteries", Electrochimica Acta **439**, 141644 (2023).

[37] C. Zhang, Z. Niu, S. Peng, Y. Ding, L. Zhang, X. Guo, Y. Zhao, and G. Yu, "Phenothiazine-based organic catholyte for high-capacity and long-life aqueous redox flow batteries", Advanced Materials **31**, 1901052 (2019).

[38] T. Kong, J. Li, W. Wang, X. Zhou, Y. Xie, J. Ma, X. Li, and Y. Wang, "Enabling long-life aqueous organic redox flow batteries with a highly stable, low redox potential phenazine anolyte", ACS Applied Materials & Interfaces **16**, 752–760 (2024).

[39] M. R. Gerhardt, L. Tong, R. Gómez-Bombarelli, Q. Chen, M. P. Marshak, C. J. Galvin, A. Aspuru-Guzik, R. G. Gordon, and M. J. Aziz, "Anthraquinone derivatives in aqueous flow batteries", Advanced Energy Materials **7**, 1601488 (2017).

[40] S. Jin, Y. Jing, D. G. Kwabi, Y. Ji, L. Tong, D. De Porcellinis, M.-A. Goulet, D. A. Pollack, R. G. Gordon, and M. J. Aziz, "A water-miscible quinone flow battery with high volumetric capacity and energy density", ACS Energy Letters **4**, 1342–1348 (2019).

[41] C. Wang et al., "Highly water-soluble 6-quinoxalinecarboxylic acid for high-voltage aqueous organic redox flow batteries", ACS Applied Energy Materials **5**, 10379–10384 (2022).

[42] X. Liu, T. Li, C. Zhang, and X. Li, "Benzidine derivatives: a class of high redox potential molecules for aqueous organic flow batteries", Angewandte Chemie International Edition **62**, e202307796 (2023).

[43] G. S. Nambafu, K. Siddharth, C. Zhang, T. Zhao, Q. Chen, K. Amine, and M. Shao, "An organic bifunctional redox active material for symmetric aqueous redox flow battery", Nano Energy **89**, 106422 (2021).